drones

MDPI

Article

Attitude Control of a Mass-Actuated Fixed-Wing UAV Based on Adaptive Global Fast Terminal Sliding Mode Control

Laohu Yuan [1,*], Jinxin Zheng [1], Xiaoguang Wang [2] and Le Ma [2]

[1] College of Aerospace Engineering, Shenyang Aerospace University, Shenyang 110136, China; zhengjinxin@stu.sau.edu.cn
[2] College of Aeronautical Engineering, Anyang Vocational and Technical College, Anyang 455000, China; wangxiaoguang@stu.sau.edu.cn (X.W.); male2@stu.sau.edu.cn (L.M.)
* Correspondence: ylhhit@sau.edu.cn

Abstract: Compared with traditional control methods, moving mass control (MMC) enhances the aerodynamic efficiency and stealth performance of fixed-wing unmanned aerial vehicles (FWUAVs), thereby facilitating their broader application in military and civilian fields. Nevertheless, this approach increases system complexity, nonlinearity, and coupling characteristics. To address these challenges, a novel attitude controller is proposed using adaptive global fast terminal sliding mode (GFTSM) control. Firstly, a dynamic model is established based on aerodynamics, flight dynamics, and moving mass dynamics. Secondly, to improve transient and steady-state responses, prescribed performance control (PPC) is adopted, which enhances the controller's adaptability for mass-actuated aircraft. Thirdly, a fixed-time extended state observer (FTESO) is utilized to solve the inertial coupling issue caused by mass block movement. Additionally, the performance of the entire control system is rigorously proven through the Lyapunov function. Finally, numerical simulations of the proposed controller are compared with those of PID and linear ADRC in three different conditions: ideal conditions, fixed aerodynamic parameters, and nonlinear aerodynamic parameter changes. The results indicate that the controller effectively compensates for the system's uncertainty and unknown disturbances, ensuring rapid and accurate tracking of the desired commands.

Keywords: moving mass control; attitude control; adaptive global fast terminal sliding mode; parameter perturbation

Citation: Yuan, L.; Zheng, J.; Wang, X.; Ma, L. Attitude Control of a Mass-Actuated Fixed-Wing UAV Based on Adaptive Global Fast Terminal Sliding Mode Control. *Drones* **2024**, *8*, 305. https://doi.org/10.3390/drones8070305

Academic Editor: Oleg Yakimenko

Received: 10 May 2024
Revised: 1 July 2024
Accepted: 2 July 2024
Published: 8 July 2024

1. Introduction

FWUAVs, with their unique advantages of a simple structure, longer flight range, and faster flight speed, have been widely utilized in military and civilian fields such as battlefield surveillance, environmental monitoring, and forest fire prevention [1,2]. Currently, the control strategy for FWUAVs primarily focuses on rudder surface control schemes and propeller differential direct force control schemes. However, the traditional aerodynamic surface control scheme has encountered a series of issues in its practical application. In particular, when a large number of movable aerodynamic surfaces are deflected, the combined effect of lift and wing weight leads to a significant change in airfoil camber. This not only increases flight drag and reduces aerodynamic efficiency but also impacts the flight performance and stealth design of FWUAVs. Although propeller differential control is another good scheme for controlling FWUAVs, its complex thrust distribution, and high energy consumption characteristics have become bottlenecks, which restrict its widespread application.

Aiming at resolving the above problems, the MMC scheme has become a feasible alternative to address the control challenges faced by FWUAVs. This control method allows for precise control of the aircraft's flying attitude by making modifications to its center of mass. As a result, it improves aerodynamic efficiency, reduces the complexity of wing

construction, enhances stealth performance, and dramatically reduces energy consumption. Therefore, MMC has significant potential for extensive use in the area of FWUAVs.

Although MMC technology has been widely used in reentry vehicles [3], hypersonic vehicles [4], underwater vehicles [5], satellites [6], near-space vehicles [7], and other fields, research in the field of FWUAVs is still relatively limited. In the context of FWUAVs, MMC technology provides new challenges and opportunities. Due to the movement of mass blocks, the dynamic system of FWUAVs becomes more complicated, and the characteristics of time-varying, strong coupling, and strong nonlinearity become more significant. In addition, factors such as aerodynamic parameter perturbation and unmodeled system dynamics also put forward higher requirements for controller design.

Various strategies have been presented to handle aircraft control challenges, including feedback linearization [8], adaptive backstepping [9], adaptive super-twisting [10], model predictive methods [11], etc. Many studies have demonstrated that controllers based on linearized models can be applied to MMC systems to some extent. Rogers [12] studied the control of an internal moving mass system based on a missile's 7-DOF model, ignoring the nonlinear terms and disturbances in the missile's kinetic model. Wang [13] obtained the transfer function of the roll channel by simplifying the nonlinear model of a single-mass-actuated reentry vehicle. Additionally, Wang constructed the controller using the conventional coefficient technique. Erturk et al. [14,15] developed a linear gain scheduling controller to achieve attitude control in a mass-actuated FWUAV. These investigations definitively reveal the abilities of mass-actuated vehicles. However, due to the uncertainty of aerodynamic parameters and the nonlinear characteristics of system dynamics, linear control methods still face many difficulties in dealing with accurate control of MMC systems. In order to overcome such limitations, the design of a nonlinear controller has become the focus of researchers. Menon et al. [16] designed a finite-horizon, robust integrated guidance and control system for a moving-mass actuated kinetic warhead by using feedback linear dynamics and generated a nonlinear feedback solution by using a multi-stepping algorithm. Gao et al. [17] designed an attitude tracking control system for a reentry warhead by combining sliding mode control theory with the feedback linearization technique. Although feedback linearization makes up for the faults of linearization approaches to a certain extent, accurate dynamic modeling is essential to maintaining the nonlinear dynamic characteristics of the system. Furthermore, adaptive control methods have also been developed for MMC systems, such as adaptive backstepping [18] and L1 adaptive control [19]. Gao et al. [20] introduced an adaptive control technique based on immersion and invariance theory that successfully followed the reference angle of attack instruction. Chen et al. [21] designed an adaptive controller with NussBaum gain based on the backstepping approach to assure the asymptotic stability of the closed-loop system. Although these methods can address nonlinear problems to some extent, their effectiveness in handling unmodeled dynamics and external disturbances is limited.

For nonlinear systems, the formulation of the model significantly influences the convergence time in finite time, which varies with different initial conditions. The fixed-time control technique emerges as a viable option for precisely determining convergence time independent of initial conditions. A scheme combining fixed-time control and sliding mode control has been designed and applied. Saim Ahmed et al. [22] proposed an adaptive fractional order sliding mode controller (AFtNTSM) for the fixed-time control and stability of a nonlinear uncertain disturbance manipulator. AFtNTSM's convergence time is independent of the initial environment and can be accurately evaluated. An adaptive fixed-time fractional integral control method is proposed for externally disturbed Euler–Lagrange systems in reference [23]. This method combines fractional calculus with integral sliding mode control and has fast convergence, smooth non-singular control inputs and timing stability. Saim Ahmed [24] designed an adaptive fixed-time control strategy for nonlinear systems with external disturbances. The fixed-time terminal sliding mode control (FxSMC) technique is introduced, offering rapid convergence, smooth control inputs, and fixed-time stability. Reference [25] proposed a time-delay estimation scheme (TDE) for

nonlinear robotic systems with uncertainties and disturbances, employing fractional-order fixed-time sliding mode control (TDEFxFSMC) and their results show that the TDEFxFSMC scheme is effective and has a fast convergence speed. It is evident that the combination of fixed-time control technology and sliding mode control technology is widely employed for certain nonlinear systems, demonstrating significant advantages in addressing nonlinear uncertainties and external disturbances.

Given this, this paper performs a thorough study on the dual-channel mass-actuated FWUAV, and a mass block is employed in the lateral and longitudinal channels to, respectively, replace the UAV's ailerons and elevators to achieve delicate control of the UAV's attitude. Based on the Lagrange equation in the quasi-coordinate, a dynamic model is established based on aerodynamics, flight dynamics, and moving mass dynamics, which offers a strong theoretical foundation for the subsequent controller design. In order to improve the adaptability and anti-interference ability of the system, an adaptive GFTSM controller is developed in this paper. By introducing PPC theory, the controller can ensure the system has good transient and steady-state performance, so as to improve its adaptability on a mass-actuated aircraft. Aimed at the inertial coupling problem caused by mass block movement, a FTESO is introduced in this paper, which can rapidly and accurately observe and eliminate the uncertainty of the system in a short time and effectively compensate for the influence of factors such as aerodynamic parameter perturbation and system unknown terms. Then, the stability of the closed-loop system is analyzed using Lyapunov theory. The controller is finally simulated and compared with PID and linear ADRC. The simulation results demonstrate that the controller given in this study has outstanding performance under ideal conditions, fixed-parameter perturbation, and nonlinear parameter perturbation, and its effectiveness in practical application is verified.

The main contributions of this paper can be summarized as follows:

(1) Based on the Lagrange equation in quasi-coordinate form, a complete dynamics model of the mass-actuated FWUAV is established to describe the flight state of the aircraft.

(2) A FTESO is proposed to monitor and eliminate the uncertainty and total disturbance of the dual-channel mass-actuated FWUAV system, ensuring rapid and accurate response and tracking of the flight target attitude.

(3) An adaptive GFTSM controller is proposed to prevent chatter generated by sliding mode switching. Combined with PPC, it limits the sliding mode surface, improving controller robustness, and anti-interference capability and prove more adaptable to mass-actuated FWUAVs.

2. Mathematical Model and Dynamic Characteristics

2.1. MMC Strategy

This section presents a FWUAV utilizing MMC technology. Figure 1 depicts the fundamental layout of a mass-actuated FWUAV. There are two masses, block 1 and block 2, positioned in the fuselage and wing, respectively, with one block in the longitudinal direction and the other in the lateral direction. The displacement of block 1 produces the pitching moment that induces a pitching motion in the UAV, effectively replacing the function of the elevator. The displacement of block 2 provides the rolling moment that steers the UAV into a rolling movement, taking the place of the ailerons. The sliding rails of the moving mass are parallel to the aircraft coordinate system's x and y axes. This paper focuses on the control method of a mass-actuated FWUAV without considering the design details of the moving mass structure.

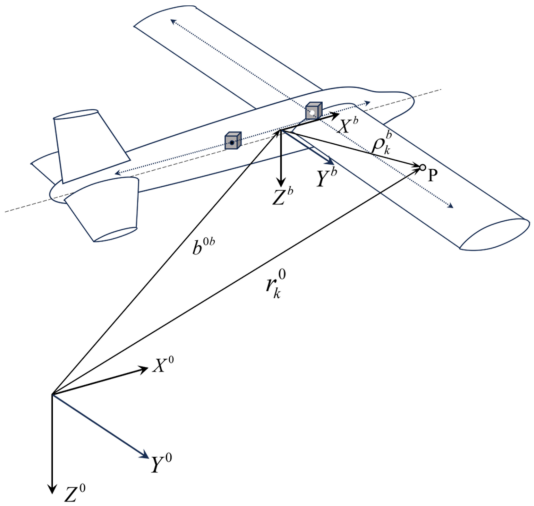

Figure 1. Reference frame configuration of the mass-actuated FWUAV.

2.2. Motion Model

This section considers the mass-actuated FWUAV proposed in this paper as a multi-rigid body system. The mass of each mass point on the body of the UAV (excluding the block) is denoted as m_0. The masses of each mass point on the two blocks are defined as m_1 and m_2, respectively. The inertial coordinate system is fixed to the Earth, which is represented by $O^0X^0Y^0Z^0$, while the unit vector X^0 points due north, Y^0 points due east, and Z^0 points towards the center of the Earth or straight down. The body coordinate system, denoted by $O^bX^bY^bZ^b$, has its origin at the center of mass of the UAV body (excluding the block). X^b points towards the head of the aircraft, Y^b points towards the right wing, and Z^b points towards the belly of the aircraft.

The position vector of the origin O^b of the body coordinate system in the inertial coordinate system is defined as $\boldsymbol{b}^{0b} = \left[X^{0b}, Y^{0b}, Z^{0b}\right]$. The Euler angle, with respect to the inertial coordinate system $O^0X^0Y^0Z^0$, is denoted by $\boldsymbol{\Theta}^{0b} = \left[\phi^{0b}, \theta^{0b}, \psi^{0b}\right]$, and the generalized coordinate is defined as $\boldsymbol{q} = [q_1, q_2, q_3, q_4, q_5, q_6] = \left[X^{0b}, Y^{0b}, Z^{0b}, \phi^{0b}, \theta^{0b}, \psi^{0b}\right]$, giving $\dot{\boldsymbol{q}} = \left[\dot{\boldsymbol{b}}^{0b}, \dot{\boldsymbol{\Theta}}^{0b}\right]$. The velocity and angular velocity vectors in the body coordinate system are defined as $\boldsymbol{v}^b = [u, v, w]$ and $\boldsymbol{\omega}^{b0} = [p, q, r]$, respectively. The array of sensors is described as $\ddot{\boldsymbol{y}} = \left[\dot{\boldsymbol{v}}^b, \dot{\boldsymbol{\omega}}^{b0}\right]$, then $\dot{\boldsymbol{y}} = \left[\boldsymbol{v}^b, \boldsymbol{\omega}^{b0}\right]$. Their relationship is as follows:

$$\dot{\boldsymbol{q}} = \boldsymbol{H}\dot{\boldsymbol{y}} \tag{1}$$

$$\boldsymbol{H} = \begin{bmatrix} \left(\boldsymbol{A}^{b0}\right)^T & 0 \\ 0 & \left(\boldsymbol{D}^{b0}\right)^T \end{bmatrix} \tag{2}$$

where $\boldsymbol{A}^{b0} = \begin{bmatrix} c\theta c\psi & c\theta s\psi & -s\theta \\ (-c\phi s\psi + s\phi s\theta c\psi) & (c\phi c\psi + s\phi s\theta s\psi) & s\phi c\theta \\ (s\phi s\psi + c\phi s\theta c\psi) & (-s\phi c\psi + c\phi s\theta s\psi) & c\phi c\theta \end{bmatrix}$ is the rotation matrix, $\boldsymbol{D}^{b0} = \begin{bmatrix} 1 & 0 & -\sin\theta \\ 0 & \cos\phi & \sin\phi\cos\theta \\ 0 & -\sin\phi & \cos\phi\cos\theta \end{bmatrix}$ is the transformation matrix, and $cx \triangleq \cos x$ and $sx \triangleq \sin x$.

2.3. Dynamic Model

The Lagrange equation in quasi-coordinate form can be utilized to express the flight state of a mass-actuated fixed-wing UAV.

$$\left[\frac{d}{dt}\left(\frac{\partial \boldsymbol{T}}{\partial \dot{\boldsymbol{y}}}\right) - \frac{\partial \boldsymbol{T}}{\partial \boldsymbol{y}}\boldsymbol{H}^T\dot{\boldsymbol{H}} - \frac{\partial \boldsymbol{T}}{\partial \boldsymbol{q}}\boldsymbol{H}\right]^T = \boldsymbol{F} + \overline{\boldsymbol{F}} \tag{3}$$

The total kinetic energy of the UAV is represented by $\boldsymbol{T}$, while $\boldsymbol{F}$ represents the total force acting on the UAV. $\overline{\boldsymbol{F}}$, on the other hand, represents the total constraint force.

Point P is selected on the UAV. $\boldsymbol{\rho}_k^b$ represents the position vector of point P in the body coordinate system, and its mass is $m_k (k = 0, 1, 2)$.

The position vector of point P in the inertial coordinate system can be written as follows:

$$\boldsymbol{r}_k^0 = \boldsymbol{b}^{0b} + \boldsymbol{A}^{0b}\boldsymbol{\rho}_k^b \tag{4}$$

The derivation gives:

$$\dot{\boldsymbol{r}}_k^0 = \dot{\boldsymbol{b}}^{0b} + \dot{\boldsymbol{A}}^{0b}\boldsymbol{\rho}_k^b + \boldsymbol{A}^{0b}\dot{\boldsymbol{\rho}}_k^b = \dot{\boldsymbol{b}}^{0b} - \boldsymbol{A}^{0b}\widetilde{\boldsymbol{\rho}}_k^b\boldsymbol{\omega}^{b0} + \boldsymbol{A}^{0b}\dot{\boldsymbol{\rho}}_k^b \tag{5}$$

where (~) represents an operator that converts a vector to its antisymmetric matrix representation (i.e., $\widetilde{\boldsymbol{x}}\boldsymbol{y} = \boldsymbol{x} \times \boldsymbol{y} \quad \forall \boldsymbol{x}, \boldsymbol{y} \in \mathbb{R}^3$).

Then, the total kinetic energy of the UAV can be represented as follows:

$$\boldsymbol{T} = \frac{1}{2}\left[\int_{V_b} \rho_0 \left(\dot{\boldsymbol{r}}_0^0\right)^T \dot{\boldsymbol{r}}_0^0 dV_b + \int_{V_1} \rho_1 \left(\dot{\boldsymbol{r}}_1^0\right)^T \dot{\boldsymbol{r}}_1^0 dV_1 + \int_{V_2} \rho_2 \left(\dot{\boldsymbol{r}}_2^0\right)^T \dot{\boldsymbol{r}}_2^0 dV_2\right] \tag{6}$$

Substituting Equations (2) and (6) into Equation (3) yields:

$$\boldsymbol{F} + \overline{\boldsymbol{F}} = \begin{bmatrix} \boldsymbol{M}_b & -\boldsymbol{S}_b \\ \boldsymbol{S}_b & \boldsymbol{J}_b \end{bmatrix}\ddot{\boldsymbol{y}} + \begin{bmatrix} \boldsymbol{M}_b\widetilde{\boldsymbol{\omega}}^{b0} & -\left(\widetilde{\boldsymbol{\omega}}^{b0}\boldsymbol{S}_b + 2\dot{\boldsymbol{S}}_b\right) \\ \boldsymbol{S}_b\widetilde{\boldsymbol{\omega}}^{b0} & \widetilde{\boldsymbol{\omega}}^{b0}\left(\boldsymbol{J}_b - 2\Sigma\widetilde{\boldsymbol{\rho}}_k^b\dot{\widetilde{\boldsymbol{\rho}}}_k^b\right) \end{bmatrix}\dot{\boldsymbol{y}} + \begin{bmatrix} \Sigma m_k\ddot{\boldsymbol{\rho}}_k^b \\ \Sigma m_k\widetilde{\boldsymbol{\rho}}_k^b\ddot{\boldsymbol{\rho}}_k^b \end{bmatrix} \tag{7}$$

As there are no constraints on the coordinates $\boldsymbol{y}$, the generalized constraint force is $\overline{\boldsymbol{F}} = 0$, where $\widetilde{\boldsymbol{\omega}}^{b0}$ is the antisymmetric matrix:

$$\widetilde{\boldsymbol{\omega}}^{b0} = \begin{bmatrix} 0 & -r & q \\ r & 0 & -p \\ -q & p & 0 \end{bmatrix} \tag{8}$$

$$\boldsymbol{M}_b = \boldsymbol{1}\sum_{k=1}^{N_b} m_k \tag{9}$$

$$\boldsymbol{S}_b = \sum_{k=1}^{N_b} m_k\widetilde{\boldsymbol{\rho}}_k^b \tag{10}$$

$$\boldsymbol{J}_b = -\sum_{k=1}^{N_b} m_k\widetilde{\boldsymbol{\rho}}_k^b\widetilde{\boldsymbol{\rho}}_k^b \tag{11}$$

The total external force on the left side of Equation (7) may be separated into gravity, aerodynamic force, and engine thrust.

$$\boldsymbol{F} = \begin{bmatrix} \boldsymbol{F}_G \\ \boldsymbol{M}_G \end{bmatrix} + \begin{bmatrix} \boldsymbol{F}_{aero} \\ \boldsymbol{M}_{aero} \end{bmatrix} + \begin{bmatrix} \boldsymbol{F}_T \\ \boldsymbol{M}_T \end{bmatrix} \tag{12}$$

The terms in the above equation may be shown as $\boldsymbol{F}_G = \boldsymbol{M}_b\boldsymbol{A}^{b0}\boldsymbol{G}$, $\boldsymbol{M}_G = \boldsymbol{S}_b\boldsymbol{A}^{b0}\boldsymbol{G}$, $\boldsymbol{F}_T = \boldsymbol{F}_{motor}$, and $\boldsymbol{M}_T = 0$, where $\boldsymbol{G} = [0, 0, g]$ and g is the acceleration of gravity.

In the body coordinate system, $\boldsymbol{F}_{aero}$ represents the aerodynamic force. However, it is more convenient to express the aerodynamic force in the velocity coordinate system. The relationship between the two can be expressed as follows:

$$\boldsymbol{F}_{aero} = \boldsymbol{A}^{bw} \boldsymbol{f}_{aero} \tag{13}$$

where $\boldsymbol{A}^{bw} = \begin{bmatrix} \cos\beta\cos\alpha & -\sin\beta\cos\alpha & -\sin\alpha \\ \sin\beta & \cos\beta & 0 \\ \cos\beta\sin\alpha & -\sin\beta\sin\alpha & \cos\alpha \end{bmatrix}$.

$\boldsymbol{f}_{aero}$ is the aerodynamic force in the velocity coordinate system. α and β are the angles of attack and sideslip. We define $\boldsymbol{X}$, $\boldsymbol{Y}$, and $\boldsymbol{Z}$ as drag, lift, and lateral forces, respectively.c_{x0}, c_{x1}, c_{x2}, c_{x3}, c_{y0}, c_{y1}, c_{y2}, c_{y3}, c_z^{β}, m_{z0}, m_x^{α}, m_y^{β}, m_x^{p}, m_y^{q}, and m_z^{r} are the relevant aerodynamic coefficients, $q_{air} = \frac{1}{2}\rho_{air} V_w^2$ is atmospheric pressure, where ρ_{air} and V_w are the atmospheric density and airspeed, respectively, while, c and S are the mean aerodynamic chord length and the wing reference area, respectively. Ma is the Mach number.

Then, according to the principles of aerodynamics, $\boldsymbol{F}_{aero}$ and $\boldsymbol{M}_{aero}$ can be expressed as:

$$\boldsymbol{F}_{aero} = \boldsymbol{A}^{bw} \begin{bmatrix} -\boldsymbol{X} \\ \boldsymbol{Y} \\ \boldsymbol{Z} \end{bmatrix} = \boldsymbol{A}^{bw} \begin{bmatrix} -\left(c_{x0} + c_{x1}\alpha^2 + c_{x2}e^{c_{x3}Ma}\right) \\ c_{y0} + c_{y1}\alpha + c_{y2}e^{c_{y3}Ma} \\ c_z^{\beta}\beta \end{bmatrix} q_{air} S \tag{14}$$

$$\boldsymbol{M}_B = \begin{bmatrix} M_{Bx} \\ M_{By} \\ M_{Bz} \end{bmatrix} = \begin{bmatrix} m_x^{p} pc/(2V_w) \\ m_y^{\beta}\beta + m_y^{q} qc/V_w \\ m_{z0} + m_z^{\alpha}\alpha + m_z^{r} rc/V_w \end{bmatrix} q_{air} Sc \tag{15}$$

2.4. Open-Loop Simulation

The block is moved in a prescribed manner to observe the dynamic response of the UAV dynamics model. In reference [26], the effects of different deformation rates on the roll and pitch channels are studied. The motion forms of the mass blocks in the pitch and roll channels are illustrated in Figures 2 and 3, respectively.

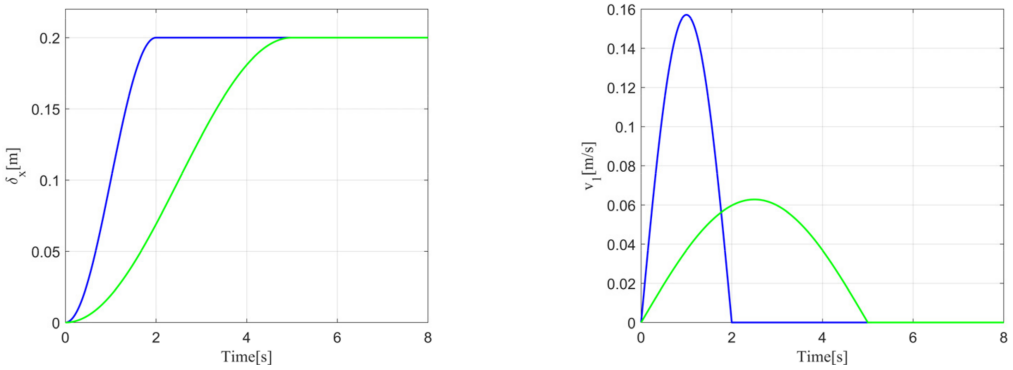

(**a**) (**b**)

Figure 2. Sliding block motion in pitch channel. (**a**) The displacement of the block in the pitch channel. State 1 shows the block moving from its initial position to a 0.2 m position within 2 s, indicated by a solid blue line. State 2 shows the block moving from its initial position to a 0.2 m position within 5 s, indicated by a solid green line; (**b**) The corresponding velocities for these two states.

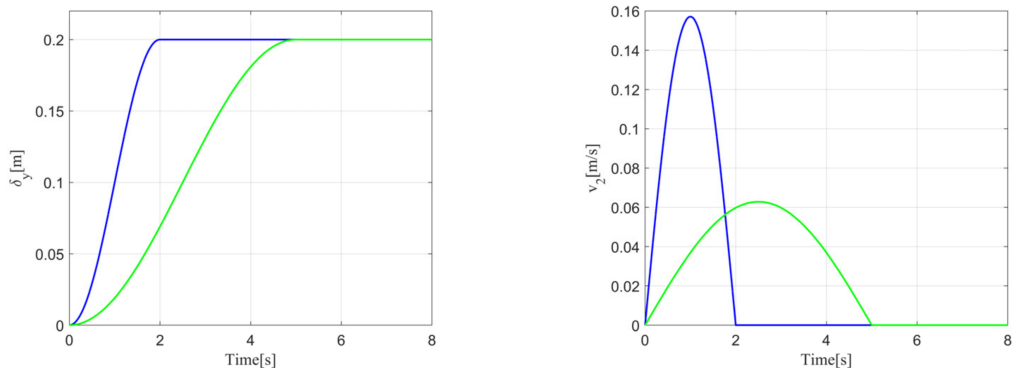

(**a**) (**b**)

Figure 3. Sliding block motion in roll channel. (**a**) The displacement of the block in the roll channel. State 1 shows the block moving from its initial position to a 0.2 m position within 2 s, indicated by a solid blue line. State 2 shows the block moving from its initial position to a 0.2 m position within 5 s, indicated by a solid green line; (**b**) The corresponding velocities for these two states.

The Figure 4 displays the open-loop dynamic responses of each mass block when executing commands. The initial condition is for the vehicle to fly straight and level in a static standard environment at an initial speed of 5 m/s. The two blocks individually reach the designated place in the motion form of the above figures. In this simulation, it is discovered that when the mass block reaches the prescribed point at a faster speed, the timing of roll angle change is early. The pitch channel is less obvious. The velocity of the mass blocks has minimal impact on the pitch channel, but it significantly influences the roll channel.

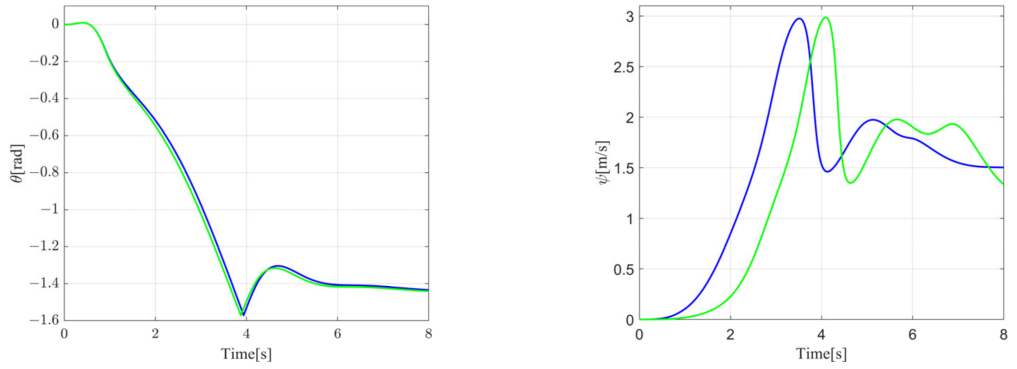

(**a**) (**b**)

Figure 4. Open−loop responses of two channels. (**a**) The change of pitch angle under two states in the pitch channel; (**b**) The change of roll angle under two states in the roll channel.

3. Design of the Controller

The current section presents a complete explication of the design process for adaptive GFTSM control based on PPC methodology while also introducing the design of the FTESO. The primary control objective is to achieve precise attitude control in the presence of significant coupling, nonlinearity, system uncertainty, and external disturbances. Figure 5 displays the whole control approach applied for the mass-actuated FWUAV.

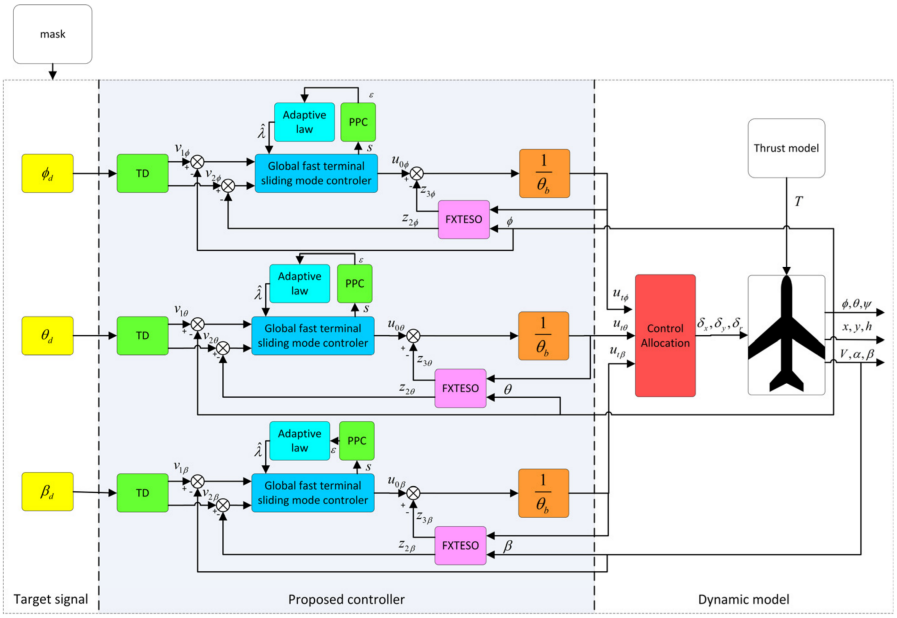

Figure 5. Proposed flight control structure.

3.1. Design of FTESO

3.1.1. Preliminaries

Prior to designing the FTESO, some definitions and lemmas must first be introduced. Assuming that the following system exists:

$$\dot{x} = f(x(t)), x \in \mathbb{R}^n, x(0) = x_0 \tag{16}$$

where $f : \mathbb{R}^n \to \mathbb{R}^n$ represents a nonlinear function.

Definition 1 ([27]). *A sufficient condition to ensure finite-time stability of Equation (16) is that the initial origin of the system is Lyapunov stable, then there exists a convergence time function $T_f : \mathbb{R}^n \to \mathbb{R}^n$ such that for every $x_0 \in \mathbb{R}^n$, it is concluded that the $x(t, x_0)$ of Equation (16) satisfies $\lim_{t \to T_f(x_0)} x(t, x_0) = 0$.*

Definition 2 ([27,28]). *A sufficient condition to ensure that Equation (16) is stable in fixed time is that it is globally stable in finite time and converges to the origin within the bounded convergence time $T_{(x_0)}$. Then, there is a positive constant T_m such that $T_{(x_0)}$ satisfies $T_{(x_0)} < T_m$.*

Lemma 1 ([29]). *If there is a continuous function $V(x) : \boldsymbol{D} \to \mathbb{R}$ and it is positive and infinite, then there will also be real numbers d and κ that satisfy $d > 0$ and $\kappa \in (0, 1)$ such that:*

$$\dot{V}(x) + d(V(t))^{\kappa} \leq 0, x \in U \backslash \{0\} \tag{17}$$

where $U \subset D$ is an open neighborhood.

Then, the origin of System (16) is finite-time stable, and the continuous settling time function T_f satisfies:

$$T_f \leq \frac{(V(x))^{(1-\kappa)}}{d(1-\kappa)} \tag{18}$$

In addition, if $D = \mathbb{R}^n$, V is appropriate and $\dot{V}$ is negative on $\mathbb{R}^n \backslash \{0\}$, hence, the origin of System (16) is a globally finite-time stable equilibrium.

Lemma 2 ([27,30]). *Consider the following system:*

$$\begin{cases} \dot{z}_1 = z_2 - k_1 sig^{\alpha_1}(z_1) - \kappa_1 sig^{\beta_1}(z_1) \\ \dot{z}_2 = z_3 - k_2 sig^{\alpha_2}(z_1) - \kappa_2 sig^{\beta_2}(z_1) \\ \vdots \\ \dot{z}_{n-1} = z_n - k_{n-1} sig^{\alpha_{n-1}}(z_1) - \kappa_{n-1} sig^{\beta_{n-1}}(z_1) \\ \dot{z}_n = -k_n sig^{\alpha_n}(z_1) - \kappa_n sig^{\beta_n}(z_1) \end{cases} \tag{19}$$

where $\alpha_i \in (0,1), \beta_i > 1 (i = 1, \cdots, n)$ *and satisfies* $\alpha_i = i\alpha - (i-1), \beta_i = i\beta - (i-1)$ $(\mathrm{i} = 1, \cdots, n), \alpha \in (1-\varepsilon, 1), \quad \beta \in (1, 1+v)$. ε *and* v *are sufficiently small positive numbers. The observer gains* $k_i, \quad \kappa_i \quad (i = 1, \cdots, n)$ *form the following Hurwitz matrixes:*

$$\boldsymbol{A}_1 = \begin{bmatrix} -k_1 & 1 & 0 & \cdots & 0 \\ -k_2 & 0 & 1 & \cdots & 0 \\ \vdots & & & & \\ -k_{n-1} & 0 & 0 & \cdots & 1 \\ -k_n & 0 & 0 & \cdots & 0 \end{bmatrix}, \boldsymbol{A}_2 = \begin{bmatrix} -\kappa_1 & 1 & 0 & \cdots & 0 \\ -\kappa_2 & 0 & 1 & \cdots & 0 \\ \vdots & & & & \\ -\kappa_{n-1} & 0 & 0 & \cdots & 1 \\ -\kappa_n & 0 & 0 & \cdots & 0 \end{bmatrix}.$$

System (19) is fixed-time stable, and the fixed time is as follows:

$$T \leq \frac{\lambda_{\max}^{\rho}(P_1)}{r_1 \rho} + \frac{1}{r_2 \sigma Y^{\sigma}} \tag{20}$$

where $\rho = 1 - \alpha, \sigma = \beta - 1, r_1 = \lambda_{\min}(\boldsymbol{Q}_1)/\lambda_{\max}(\boldsymbol{P}_1), r_2 = \lambda_{\min}(\boldsymbol{Q}_2)/\lambda_{\max}(\boldsymbol{P}_2), 0 < Y \leq \lambda_{\min}(\boldsymbol{P}_2)$. $\boldsymbol{P}_1, \boldsymbol{Q}_1, \boldsymbol{P}_2$, *and* $\boldsymbol{Q}_2$ *are symmetric positive definite and satisfy* $\boldsymbol{P}_1\boldsymbol{A}_1 + \boldsymbol{A}_1^T\boldsymbol{P}_1 = -\boldsymbol{Q}_1$ *and* $\boldsymbol{P}_2\boldsymbol{A}_2 + \boldsymbol{A}_2^T\boldsymbol{P}_2 = -\boldsymbol{Q}_2$.

Assumption 1. *f_u is continuously differentiable with respect to time and satisfies that $|f_u| \leq D_{u1}$ and $\dot{f}_u \leq D_{u2}$, where D_{u1} and D_{u2} are known positive constants.*

3.1.2. Design of the Observer

Using the pitch channel of the mass-actuated FWUAV as an example and taking into account the unknown functions and model deviations of the system, including disturbance and coupling terms, the dynamic equation can be rewritten as:

$$\begin{cases} \dot{x}_1 = x_2 \\ \dot{x}_2 = x_3 + bu \\ \dot{x}_3 = \dot{f}_u \end{cases} \tag{21}$$

where f_u is the unknown function and lumped disturbance of the system, and the control parameter b can be obtained through experience. u represents the control input. The relevant variables of the UAV dynamics equation transformed into Equation (21) are provided in Appendix A.

It can be seen that the initial dynamics of the system are approximated by the second-order integral system, which is perturbed by the total disturbance. The main issue is to estimate and eliminate the total disturbance to prevent the system from deviating from the expectation. It can be seen from Equation (21) that f_u is regarded as a system state variable $x_3 = f_u$.

Based on the FTESO presented in reference [27], the FTESO of this paper can be described as follows:

$$\begin{cases} e_1 = z_1 - x_1 \\ \dot{z}_1 = z_2 - k_1 \lfloor e_1 \rceil^{a_1} - m_1 \lfloor e_1 \rceil^{b_1} \\ \dot{z}_2 = z_3 - k_2 \lfloor e_1 \rceil^{a_2} - m_2 \lfloor e_1 \rceil^{b_2} \\ \dot{z}_3 = -k_3 \lfloor e_1 \rceil^{a_3} - m_3 \lfloor e_1 \rceil^{b_3} + K\mathrm{sgn}(e_1) \end{cases} \tag{22}$$

We define $\lfloor x \rceil^k = |x|^k \mathrm{sgn}(x)$, where $k \in \mathbb{R}$ and $\mathrm{sgn}(\cdot)$ is the sign function. $a_i \in (0,1)$, $b_i > 1$, $i = 1,2,3$, and it satisfies $a_1 = a$, $a_2 = 2a - 1$, $a_3 = 3a - 2$, $b_1 = b$, $b_2 = 2b - 1$, $b_3 = 3b - 2$ k_i and m_i, $(i = 1,2,3)$ represent the observer gains, respectively. The observation error of the FTESO can be expressed as:

$$\begin{cases} e_1 = z_1 - x_1 \\ e_2 = z_2 - x_2 \\ e_3 = z_3 - f_u \end{cases} \tag{23}$$

The relationship can be represented as follows:

$$\begin{cases} \dot{e}_1 = e_2 - k_1 \lfloor e_1 \rceil^{a_1} - m_1 \lfloor e_1 \rceil^{b_1} \\ \dot{e}_2 = e_3 - k_2 \lfloor e_1 \rceil^{a_2} - m_2 \lfloor e_1 \rceil^{b_2} \\ \dot{e}_3 = -k_3 \lfloor e_1 \rceil^{a_3} - m_3 \lfloor e_1 \rceil^{b_3} - K\mathrm{sgn}(e_1) + \dot{f}_u \end{cases} \tag{24}$$

The following theorem is given and proven:

Theorem 1. *For any channel of FWUAV attitude control, taking the pitch channel as an example, if a fixed-time extended state observer such as Equation (22) is designed, there will be constants $a_i \in (0,1)$, $b_i > 1$, $(i = 1,2,3)$ and the appropriate observer gain parameters $k_i, m_i (i = 1,2,3)$, and the state variables x_1 and x_2 can be observed by z_1 and z_2 within a fixed time. The observed error of the total disturbance can converge to the neighborhood of the origin in a fixed time.*

Proof of Theorem 1. According to the error model presented in Equation (24), the following observer equation can be obtained:

$$\begin{cases} \dot{e}_1 = e_2 - k_1 \lfloor e_1 \rceil^{a_1} \\ \dot{e}_2 = e_3 - k_2 \lfloor e_1 \rceil^{a_2} \\ \dot{e}_3 = -k_3 \lfloor e_1 \rceil^{a_3} \end{cases} \tag{25}$$

Define $\boldsymbol{\xi} = \left[e_1^{1/a_1}, e_2^{1/a_2}, e_3^{1/a_3} \right] \in \mathbb{R}^3$, $\boldsymbol{e}(t) = [e_1, e_2, e_3]$, then there is a symmetric positive definite matrix $\boldsymbol{Q}_1 \in \mathbb{R}^{3\times 3}$ and $\boldsymbol{P}_1$ such that:

$$\boldsymbol{A}_1^T \boldsymbol{P}_1 + \boldsymbol{P}_1 \boldsymbol{A}_1 = -\boldsymbol{Q}_1 \tag{26}$$

where $\boldsymbol{A}_1$ is the Hurwitz matrix and yields $\boldsymbol{A}_1 = \begin{bmatrix} -k_1 & 1 & 0 \\ -k_2 & 0 & 1 \\ -k_3 & 0 & 0 \end{bmatrix}$.

From the above series of definitions, $\dot{\boldsymbol{e}}(t) = \boldsymbol{A}_1 \boldsymbol{e}(t)$ can be obtained, for which $V(\boldsymbol{e}(t)) = \boldsymbol{e}^T \boldsymbol{P}_1 \boldsymbol{e}$ is selected as the Lyapunov function, and $\dot{V}(\boldsymbol{e}(t)) = -\boldsymbol{e}^T \boldsymbol{Q}_1 \boldsymbol{e} < 0$ is easily obtained. We can conclude from reference [27] that if $a \in (1 - \varepsilon_1, 1)$ is chosen for a sufficiently small $\varepsilon_1 > 0$, there exists a Lyapunov function $V_1(\boldsymbol{\xi}) = \boldsymbol{\Omega}^T \boldsymbol{P}_1 \boldsymbol{\Omega} > 0$ and $\dot{V}_1(\boldsymbol{\xi}) = \boldsymbol{\xi}^T \left(\boldsymbol{A}_1^T \boldsymbol{P}_1 + \boldsymbol{P}_1 \boldsymbol{A}_1 \right) \boldsymbol{\xi} = -\boldsymbol{\xi}^T \boldsymbol{Q}_1 \boldsymbol{\xi} \leq 0$ is satisfied. Additionally, $\dot{V}_1(\boldsymbol{\xi})$ satisfies:

$$\dot{V}_1(\boldsymbol{\xi}) \leq -\frac{\lambda_{\min}(\boldsymbol{Q}_1)}{\lambda_{\max}(\boldsymbol{P}_1)} V_1^a(\boldsymbol{\xi}) \tag{27}$$

where $\lambda_{\max}(\boldsymbol{P}_1)$ is a positive number, representing the largest eigenvalue of $\boldsymbol{P}_1$, and $\lambda_{\min}(\boldsymbol{Q}_1)$ is a positive number representing the smallest eigenvalue of $\boldsymbol{Q}_1$. By Lemma 1, System (25) is finite-time stable and the settling time is:

$$T_{1f} \leq \frac{\lambda_{\max}(\boldsymbol{P}_1)}{\lambda_{\min}(\boldsymbol{Q}_1)(1-a)} V_1^{1-a}(\boldsymbol{\xi}) \tag{28}$$

Examine the second part of Equation (24) below:

$$\begin{cases} \dot{e}_1 = e_2 - m_1 \lfloor e_1 \rceil^{a_1} \\ \dot{e}_2 = e_3 - m_2 \lfloor e_1 \rceil^{a_2} \\ \dot{e}_3 = -m_3 \lfloor e_1 \rceil^{a_3} \end{cases} \tag{29}$$

The Hurwitz matrix $\boldsymbol{A}_2$ can be written as $\boldsymbol{A}_2 = \begin{bmatrix} -m_1 & 1 & 0 \\ -m_2 & 0 & 1 \\ -m_3 & 0 & 0 \end{bmatrix}$.

The linear system $\dot{\boldsymbol{e}}(t) = \boldsymbol{A}_2 \boldsymbol{e}(t)$ is asymptotically stable and $V_2(\boldsymbol{e}(t)) = \boldsymbol{e}^T \boldsymbol{P}_2 \boldsymbol{e}$ is a Lyapunov function for this system.

$\boldsymbol{P}_2$ is symmetric positive definite and satisfies

$$\boldsymbol{A}_2^T \boldsymbol{P}_2 + \boldsymbol{P}_2 \boldsymbol{A}_2 = -\boldsymbol{Q}_2 \tag{30}$$

where $\boldsymbol{Q}_2$ is also symmetric positive definite. Hence, $\dot{V}_2(\boldsymbol{e}(t))$ satisfies

$$\dot{V}_2(\boldsymbol{e}(t)) = -\boldsymbol{e}^T \boldsymbol{Q}_2 \boldsymbol{e} < 0 \tag{31}$$

Rayleigh's inequalities and relation (29) imply that $V_2(\boldsymbol{e}(t)) \leq \lambda_{\max}(\boldsymbol{P}_2)\|\boldsymbol{e}\|^2$ and $\dot{V}_2(\boldsymbol{e}(t)) \leq -\lambda_{\min}(\boldsymbol{Q}_2)\|\boldsymbol{e}\|^2$, therefore, $\dot{V}_2(\boldsymbol{e}(t)) \leq -\frac{\lambda_{\min}(\boldsymbol{Q}_2)}{\lambda_{\max}(\boldsymbol{P}_2)} V_2(\boldsymbol{e}(t))$.

Define $\boldsymbol{\xi}_2 = \left[e_1^{1/b_1}, e_2^{1/b_2}, e_3^{1/b_3}\right] \in \mathbb{R}^3$, if $b \in (1, 1+\varepsilon_2)$ is chosen for a sufficiently small $\varepsilon_2 > 0$, there exists a Lyapunov function $V_2(\boldsymbol{\xi}_2) = {\boldsymbol{\xi}_2}^T \boldsymbol{P}_2 \boldsymbol{\xi}_2$ and $\dot{V}_2(\boldsymbol{\xi}_2) = {\boldsymbol{\xi}_2}^T \left(\boldsymbol{A}_2^T \boldsymbol{P}_2 + \boldsymbol{P}_2 \boldsymbol{A}_2\right) \boldsymbol{\xi}_2 = -{\boldsymbol{\xi}_2}^T \boldsymbol{Q}_2 \boldsymbol{\xi}_2 < 0$ is satisfied. Therefore, System (22) is asymptotically stable. The right side of the system (22) is a homogeneous vector field of degree $\varpi_2 = b - 1 > 0$ with respect to dilations $b_1 = b$, $b_2 = 2b - 1$, $b_3 = 3b - 2$. According to reference [27], if b is sufficiently close to 1, the full-time derivative of the Lyapunov function $V_2(\boldsymbol{\xi}_2)$ is homogeneous in e_1, e_2, e_3 of degree $1 + \varpi_2$ with respect to the same weights $b_1 = b$, $b_2 = 2b - 1$, and $b_3 = 3b - 2$. By Lemma 1, the following inequality can be obtained

$$\dot{V}_2(\boldsymbol{\xi}_2) \leq -\frac{\lambda_{\min}(\boldsymbol{Q}_2)}{\lambda_{\max}(\boldsymbol{P}_2)} V_2^b(\boldsymbol{\xi}_2) \tag{32}$$

In summary, for the observer,

$$\begin{cases} \dot{e}_1 = e_2 - k_1 \lfloor e_1 \rceil^{a_1} - m_1 \lfloor e_1 \rceil^{b_1} \\ \dot{e}_2 = e_3 - k_2 \lfloor e_1 \rceil^{a_2} - m_2 \lfloor e_1 \rceil^{b_2} \\ \dot{e}_3 = -k_3 \lfloor e_1 \rceil^{a_3} - m_3 \lfloor e_1 \rceil^{b_3} \end{cases} \tag{33}$$

According to the Lemma 2, it can be concluded that the boundary time for the observer error to converge to 0 is

$$\begin{aligned} T_B &= \frac{\lambda_{\max}^{\rho}(\boldsymbol{P}_1)}{r_1 \rho} + \frac{1}{r_2 \sigma Y^{\sigma}} \\ &= \frac{\lambda_{\max}{}^{(2-a)}(\boldsymbol{P}_1)}{\lambda_{\min}(\boldsymbol{Q}_1)(1-a)} + \frac{\lambda_{\max}(\boldsymbol{P}_2)}{\lambda_{\min}(\boldsymbol{Q}_2)(b-1)\Delta^{b-1}} \end{aligned} \tag{34}$$

When $t = T_B$, $e_1 = 0$, and e_1 remain 0 in future time. Also, for $t \geq T_B$, $e_1 = e_2 = e_3 = 0$, and $\dot{e}_1 = 0$. This shows that the following equation guarantees [31]:

$$\dot{e}_3 = K\text{sgn}(e_1) - \dot{f}_u = 0, t \geq T_B \tag{35}$$

However, e_3 is not strictly equal to 0 due to f_u. When the sufficiently small convergence domain $e_3|_{\updownarrow}$, we can have that if $e_3 > 0$, then $\dot{e}_3 \leq -K + D_{u2}$, and if $e_3 < 0$, then $\dot{e}_3 > K - D_{u2}$. K satisfies $K > D_{u2}$.

It is readily obtained that

$$\dot{e}_3 \geq K\text{sgn}(e_1) - D_{u2} \tag{36}$$

Thus, by integrating Equation (36) over time, it can be obtained that

$$\begin{aligned} e_3 &\geq (K - D_{u2}) \cdot T_{f_u} \\ e_3|_{\updownarrow} &\geq (K - D_{u2}) \cdot T_{f_u} \\ \frac{e_3|_{\updownarrow}}{K - D_{u2}} &\geq T_{f_u} \end{aligned} \tag{37}$$

Therefore, the upper bound of the FTESO convergence time in this channel is:

$$T = T_B + T_{f_u} \tag{38}$$

Theorem 1 is proved. □

When the appropriate observer parameter $a, b, k_i, m_i, (i = 1, 2, 3)$ is selected, the system state variable $x_i (i = 1, 2, 3)$ can be well estimated by $z_i (i = 1, 2, 3)$, especially $z_3 \approx x_3$.

3.2. Design of AGFTSMC Based on PPC

After catching the estimated value z_3 for the unknown disturbance, an adaptive GFTSM controller based on PPC is created in this section by combining the adaptive control theory and the sliding mode control theory for the mass-actuated FWUAV. The primary purpose is to create an appropriate control law so that the following tracking demands are satisfied:

1. $\lim_{t \to \infty} e_x = \lim_{t \to \infty} (x - x_d) = 0$;
2. The closed-loop system remains stable.

3.2.1. GFTSM Control Strategy

Since the major control purpose of this paper is attitude tracking control of the mass-actuated FWUAV system, the attitude angle errors between the real states x_1 of the system and the expected value x_d are specified as:

$$e(t) = x_1 - x_d \tag{39}$$

Define $f(x, t)$ as a known smooth function in the system, $d(x, t)$ is the unmodeled function and the external disturbance of the system, the control parameter θ_b can be obtained through experience, and $|d(x, t)| \leq L$ $(L > 0)$, then rewrite Equation (21) as:

$$\begin{cases} \dot{x}_1 = x_2 \\ \dot{x}_2 = f(x, t) + \theta_b u + z_3 \\ y = x_1 \end{cases} \tag{40}$$

To ensure the convergence of the trajectory-following errors stated above, the sliding mode surface is formulated as:

$$s(t) = \dot{e}(t) + \alpha_0 e(t) + \beta_0 e(t)^{q_0/p_0} \tag{41}$$

where α_0, β_0 are positive constants, and $p_0, q_0 (q < p)$ are positive odd numbers.

3.2.2. PPC Section

This section seeks to optimize the transient and steady-state response performance to assure convergence of the GFTSM surface to a preset region. For this objective, the PPC approach is employed, which has the following performance characteristics:

$$\begin{cases} -\delta\rho(t) < s(t) < \rho(t), & s(0) \geq 0 \\ -\rho(t) < s(t) < \delta\rho(t), & s(0) < 0 \end{cases} \tag{42}$$

where $0 \leq \delta \leq 1$ is the tuning coefficient, and the function $\rho(t)$ denotes a differentiable, bounded, and strictly positive definite decreasing function, which is presented as follows:

$$\rho(t) = (\rho_0 - \rho_\infty)e^{-lt} + \rho_\infty \tag{43}$$

where ρ_0, ρ_∞ $(\rho_0 > \rho_\infty)$ and l are positive constants. l indicates the lower bound of the rate at which the tracking error converges. The controller is rewritten based on the transformed error to ensure the smooth implementation of the prescribed performance. Therefore, the error transformed function can be expressed as follows:

$$s(t) = T(\varepsilon(t))\rho(t) \tag{44}$$

$$T(\varepsilon(t)) = \frac{\overline{\delta}e^{\varepsilon(t)} - \underline{\delta}}{e^{\varepsilon(t)} + 1} \tag{45}$$

where function $T(\varepsilon)$ is a smooth and strictly positive, satisfying $\underline{\delta} \leq T(\varepsilon) \leq \overline{\delta}$ and the conditions outlined below must be met by both $\underline{\delta}$ and $\overline{\delta}$.

$$\left(-\underline{\delta}, \overline{\delta}\right) = \begin{cases} (-\delta, 1), & if\, s(0) \geq 0 \\ (-1, \delta), & if\, s(0) < 0 \end{cases} \tag{46}$$

Hence, the homeomorphic mapping function can be written as:

$$\varepsilon(t) = \ln\left(\frac{s(t) + \underline{\delta}\rho(t)}{\overline{\delta}\rho(t) - s(t)}\right) \tag{47}$$

Derivation of the above transformed sliding mode surface is obtained as:

$$\dot{\varepsilon}(t) = \left(\frac{\overline{\delta} + \underline{\delta}}{(\underline{\delta}\rho(t) + s(t))(\overline{\delta}\rho(t) - s(t))}\right)\left(\rho(t)\dot{s}(t) - \dot{\rho}(t)s(t)\right) \tag{48}$$

where

$$H = \frac{\overline{\delta} + \underline{\delta}}{(\underline{\delta}\rho(t) + s(t))(\overline{\delta}\rho(t) - s(t))} \tag{49}$$

3.2.3. Adaptive Control Component

To enhance the dynamic response of the system and ensure its steady-state performance and anti-interference ability, it is more convenient to determine the gain of the sliding mode reaching law and reduce the complexity of control parameter adjustments. Therefore, an adaptive law is designed to replace the λ_s:

$$\dot{\hat{\lambda}}_a = \begin{cases} \varpi {\tau_a}^{-\sigma_a}\left(|\varepsilon(t)| + \eta_a e^{-|\varepsilon(t)|}\right)\sigma_a, \hat{\lambda}_a > \mu \\ \varpi {\tau_a}^{-\sigma_a}\left(|\varepsilon(t)| + \eta_a e^{-|\varepsilon(t)|}\right), else \end{cases} \tag{50}$$

where $\sigma_a = \mathrm{sgn}(\|\varepsilon(t)\|_\infty - \varepsilon_a)$. $\hat{\lambda}_a$ is the observed value of λ_s. ϖ, τ_a, and η_a are all gains and are all positive. $\mu > 0$, and it is a small normal number. It is used to guarantee that

$\lambda_s > 0$. ϖ and τ_a jointly control the adjustment speed of the adaptive law. The larger ϖ is, the smaller τ_a is, and the faster the adjustment speed is. ε_a controls the final neighborhood of the transformed sliding mode surface $\varepsilon(t)$.

Based on the concept of sliding mode control input, the GFTSM control law can be constructed as:

$$\begin{cases} \overline{u} = \overline{u}_{eq} + \overline{u}_{sw} \\ \overline{u}_{eq} = \frac{1}{H\rho(t)\theta_b}\left[H\rho(t)\left[f(x,t) - \ddot{x}_d - \alpha_0\dot{e}(t) - \beta_0\frac{d}{dt}e(t)^{q_0/p_0}\right] - H\dot{\rho}(t)s(t)\right] \\ \overline{u}_{sw} = \frac{1}{H\rho(t)\theta_b}\left[\left[\lambda_s s(t) + \gamma_s s(t)^{q/p}\right]H\rho(t)\right] \end{cases} \tag{51}$$

$$\begin{cases} u = \theta_b N(k_s)\overline{u} \\ \dot{k}_s = cs(t)H\rho(t)\theta_b\overline{u} \end{cases} \tag{52}$$

where $\lambda_s, \gamma_s, c > 0$. p and q are positive odd numbers and satisfy $q < p$. $\gamma_s = \frac{L}{\left|s(t)^{q/p}\right|} + \eta_s, \eta_s > 0$.

3.2.4. Stability Analysis of the Controller

The following definitions and lemmas are offered to facilitate the demonstration of stability.

Definition 3 ([32]). *If the function $N(x)$ satisfies the following conditions, then $N(x)$ is a Nussbaum function and satisfies the following two-sided property.*

$$\begin{cases} \lim\limits_{k_s\to\pm\infty}\sup\frac{1}{k_s}\int_0^{k_s} N(s)ds = \infty \\ \lim\limits_{k_s\to\pm\infty}\inf\frac{1}{k_s}\int_0^{k_s} N(s)ds = -\infty \end{cases} \tag{53}$$

According to the Nussbaum function definition, define the Nussbaum function as:

$$N(k_s) = {k_s}^2\cos(k_s) \tag{54}$$

where k_s is a real number.

Lemma 3 ([33]). *If $V(t)$ and $k_s(\cdot)$ are smooth functions on $\forall t \in \left[0, t_f\right)$,$V(t) \geq 0$,$N(\cdot)$ is a smooth function N, and θ_0 is a non-zero constant, if they satisfy:*

$$V(t) \leq \int_0^t \{\theta_0 N[k_s(\tau)] + 1\}\dot{k}_s(\tau)d\tau + const, \quad \forall t \in \left[0, t_f\right) \tag{55}$$

then $V(t), k_s(t)$ and $\int_0^t \{\theta_0 N[k_s(\tau)] + 1\}\dot{k}_s(\tau)d\tau$ is upper bounded in $\forall t \in \left[0, t_f\right)$.

Lemma 4 ([34]). *If $f, \dot{f} \in L_\infty$ and, $f \in L_p, p \in [1, \infty)$,then when $t \to \infty$, $f(t) \to 0$.*

Lemma 5 ([35]). *Given a nonlinear uncertain system (40) with a sliding mode surface (41), the parameter λ_a has an upper bound, i.e., there exists a positive value λ^* so that $\lambda_a < \lambda^*, \forall t > 0$.*

Theorem 2. *The flight controllers, represented by Equations (51) and (52), are designed based on the dynamics model of the mass-actuated fixed-wing UAV mentioned above. The proposed controllers keep the nonlinear system asymptotically stable.*

Proof of Theorem 2. Construct a Lyapunov function as follows:

$$V = \frac{1}{2}\varepsilon(t)^2 + \frac{1}{2h}\widetilde{\lambda}_a^2 \tag{56}$$

where $\widetilde{\lambda}_a = \hat{\lambda}_a - \lambda^*$ and λ^* is the upper bound of $\hat{\lambda}_a$; that is, $\widetilde{\lambda}_a < 0$.

The time derivative of V with respect to the Lyapunov function (56) is obtained:

$$\dot{V} = \varepsilon(t)\dot{\varepsilon}(t) + \frac{1}{h}\widetilde{\lambda}_a\dot{\widetilde{\lambda}}_a \tag{57}$$

The following is the first derivative of Equation (39) with respect to time, to obtain:

$$\dot{e}(t) = \dot{x}_1 - \dot{x}_d \tag{58}$$

Then, by taking the time derivative from Equation (58) and substituting Equation (40) into it, we can obtain:

$$\ddot{e}(t) = \ddot{x}_1 - \ddot{x}_d = f(x,t) + \theta_b u + z_3 - \ddot{x}_d \tag{59}$$

Take a time derivative of Equation (41) and obtain:

$$\dot{s}(t) = \ddot{e}(t) + \alpha_0\dot{e}(t) + \beta_0\frac{q_0}{p_0}\dot{e}(t)e(t)^{q_0/p_0-1} \tag{60}$$

Substitute Equation (59) into (60) to obtain:

$$\dot{s}(t) = f(x,t) + \theta_b u + z_3 - \ddot{x}_d + \alpha_0\dot{e}(t) + \beta_0\frac{q_0}{p_0}\dot{e}(t)e(t)^{q_0/p_0-1} \tag{61}$$

Substituting Equation (61) into (48) leads to:

$$\begin{aligned}\dot{\varepsilon}(t) \quad &= \left[\frac{\overline{\delta}+\underline{\delta}}{(\underline{\delta}\rho(t)+s(t))\left(\overline{\delta}\rho(t)-s(t)\right)}\right] \\ &\cdot\left[\rho(t)\left[f(x,t) + \theta_b u + z_3 - \ddot{x}_d + \alpha_0\dot{e}(t) + \beta_0\tfrac{q_0}{p_0}\dot{e}(t)e(t)^{q_0/p_0-1}\right] - \dot{\rho}(t)s(t)\right]\end{aligned} \tag{62}$$

With auxiliary variable (49), Equation (62) can be rewritten and organized as:

$$\begin{aligned}\dot{\varepsilon}(t) \quad &= H\Big(\rho(t)\left[f(x,t) + \theta_b u + z_3 - \ddot{x}_d + \alpha_0\dot{e}(t) + \beta_0\tfrac{q_0}{p_0}\dot{e}(t)e(t)^{q_0/p_0-1}\right] - \dot{\rho}(t)s(t)\Big) \\ &= H\rho(t)\left[f(x,t) - \ddot{x}_d + \alpha_0\dot{e}(t) + \beta_0\tfrac{q_0}{p_0}\dot{e}(t)e(t)^{q_0/p_0-1}\right] - H\dot{\rho}(t)s(t) \\ &+H\rho(t)\theta_b u + H\rho(t)z_3\end{aligned} \tag{63}$$

Now, substitute Equation (63) into Equation (57) and obtain the following result:

$$\begin{aligned}\dot{V} = \quad &\varepsilon(t)\left[H\rho(t)\left[f(x,t) - \ddot{x}_d + \alpha_0\dot{e}(t) + \beta_0\tfrac{q_0}{p_0}\dot{e}(t)e(t)^{q_0/p_0-1}\right] - H\dot{\rho}(t)s(t) + H\rho(t)\theta_b u\right] \\ &+\varepsilon(t)H\rho(t)z_3 + \tfrac{1}{h}\widetilde{\lambda}_a\dot{\widetilde{\lambda}}_a\end{aligned} \tag{64}$$

Substituting Equation (52) into Equation (64), the following is obtained:

$$\begin{aligned}\dot{V} = \quad &\varepsilon(t)\left[H\rho(t)\left[f(x,t) - \ddot{x}_d + \alpha_0\dot{e}(t) + \beta_0\tfrac{q_0}{p_0}\dot{e}(t)e(t)^{q_0/p_0-1}\right] - H\dot{\rho}(t)s(t) + H\rho(t)z_3\right] \\ &+\varepsilon(t)H\rho(t)\theta_b N(k_s)\overline{u} + \tfrac{1}{c}\dot{k}_s - \varepsilon(t)H\rho(t)\theta_b\overline{u} + \tfrac{1}{h}\widetilde{\lambda}_a\dot{\widetilde{\lambda}}_a\end{aligned} \tag{65}$$

Substituting Equation (51) into Equation (65) yields:

$$\begin{aligned}\dot{V} = \quad & \varepsilon(t)H\rho(t)\left[f(x,t) - \ddot{x}_d + \alpha_0\dot{e}(t) + \beta_0\tfrac{q_0}{p_0}\dot{e}(t)e(t)^{q_0/p_0-1}\right] - \varepsilon(t)H\dot{\rho}(t)s(t) \\ & +\varepsilon(t)H\rho(t)z_3 + \varepsilon(t)H\rho(t)N(k_s)\theta_b\overline{u} + \tfrac{1}{c}\dot{k}_s \\ & -\varepsilon(t)H\rho(t)\left[f(x,t) - \ddot{x}_d + \alpha_0\dot{e}(t) + \beta_0\tfrac{q_0}{p_0}\dot{e}(t)e(t)^{q_0/p_0-1}\right] \\ & -\varepsilon(t)H\rho(t)\left(\lambda_s s(t) + \gamma_s s(t)^{q/p}\right) + \varepsilon(t)H\dot{\rho}(t)s(t) + \tfrac{1}{h}\widetilde{\lambda}_a\dot{\widetilde{\lambda}}_a\end{aligned} \tag{66}$$

Combined with Equation (52), Equation (66) is simplified as follows:

$$\dot{V} = \frac{1}{c}\theta_b N(k_s)\dot{k}_s + \frac{1}{c}\dot{k}_s - \varepsilon(t)H\rho(t)\left(\lambda_s s(t) + \gamma_s s(t)^{q/p}\right) + \frac{1}{h}\widetilde{\lambda}_a\dot{\widetilde{\lambda}}_a \tag{67}$$

Considering the two cases $|s(t)| > \varepsilon_a$ and $|s(t)| \le \varepsilon_a$, when $|s(t)| > \varepsilon_a$, $\sigma_a = 1$, and assuming $h = \frac{\tau_a}{\varpi}$, the following derivation process can be obtained:

$$\begin{aligned}\dot{V} \quad & = \tfrac{1}{c}\theta_b N(k_s)\dot{k}_s + \tfrac{1}{c}\dot{k}_s - \varepsilon(t)H\rho(t)\left[\lambda_s s(t) + \gamma_s s(t)^{q/p} + z_3\right] + \tfrac{1}{h}\widetilde{\lambda}_a\dot{\widetilde{\lambda}}_a \\ & = \tfrac{1}{c}\theta_b N(k_s)\dot{k}_s + \tfrac{1}{c}\dot{k}_s - \varepsilon(t)H\rho(t)\left[\lambda_s s(t) + \gamma_s s(t)^{q/p} + z_3\right] + \tfrac{1}{h}\widetilde{\lambda}_a\dot{\widetilde{\lambda}}_a \\ & = \tfrac{1}{c}\theta_b N(k_s)\dot{k}_s + \tfrac{1}{c}\dot{k}_s - \varepsilon(t)H\rho(t)\left[\lambda_s s(t) + \gamma_s s(t)^{q/p} + z_3\right] \\ & +\tfrac{1}{h}\widetilde{\lambda}_a\varpi{\tau_a}^{-\sigma_a}\left(|\varepsilon(t)| + \eta_a e^{-|\varepsilon(t)|}\right)\sigma_a \\ & = \tfrac{1}{c}\theta_b N(k_s)\dot{k}_s + \tfrac{1}{c}\dot{k}_s - \varepsilon(t)H\rho(t)\left[\lambda_s s(t) + \gamma_s s(t)^{q/p} + z_3\right] \\ & +\widetilde{\lambda}_a\left(|\varepsilon(t)| + \eta_a e^{-|\varepsilon(t)|}\right)\end{aligned} \tag{68}$$

Combining Equations (42), (47), and (49) can be derived as:

$$\begin{aligned}\dot{V} \quad & = \tfrac{1}{c}\theta_b N(k_s)\dot{k}_s + \tfrac{1}{c}\dot{k}_s \\ & -\varepsilon(t)H\rho(t)\left[\lambda_s s(t) + \gamma_s s(t)^{q/p} + z_3\right] + \widetilde{\lambda}_a\left(|\varepsilon(t)| + \eta_a e^{-|\varepsilon(t)|}\right) \\ & = \ln\left(\tfrac{s(t)+\delta\rho(t)}{\overline{\delta}\rho(t)-s(t)}\right)H\rho(t)\left[-\lambda_s s(t) - \gamma_s s(t)^{q/p} - z_3\right] \\ & +\widetilde{\lambda}_a\left(|\varepsilon(t)| + \eta_a e^{-|\varepsilon(t)|}\right) + \tfrac{1}{c}\theta_b N(k_s)\dot{k}_s + \tfrac{1}{c}\dot{k}_s \\ & \le \tfrac{2s(t)H\rho(t)}{\overline{\delta}\rho(t)-s(t)}\left[-\lambda_s s(t) - \tfrac{L}{\left|s(t)^{q/p}\right|}s(t)^{q/p} - \eta_s s(t)^{q/p} - z_3\right] \\ & +\widetilde{\lambda}_a\left(|\varepsilon(t)| + \eta_s e^{-|\varepsilon(t)|}\right) + \tfrac{1}{c}\theta_b N(k_s)\dot{k}_s + \tfrac{1}{c}\dot{k}_s \\ & \le \tfrac{2H\rho(t)}{\overline{\delta}\rho(t)-s(t)}\left[-\lambda_s s(t)^2 - L|s(t)| - \eta_s s(t)^{(p+q)/p} - z_3\right] \\ & +\widetilde{\lambda}_a\left(|\varepsilon(t)| + \eta_a e^{-|\varepsilon(t)|}\right) + \tfrac{1}{c}\theta_b N(k_s)\dot{k}_s + \tfrac{1}{c}\dot{k}_s \\ & \le \tfrac{2H\rho(t)}{\overline{\delta}\rho(t)-s(t)}\left[-\lambda_s s(t)^2 - \eta_s s(t)^{(p+q)/p}\right] + \widetilde{\lambda}_a\left(|\varepsilon(t)| + \eta_a e^{-|\varepsilon(t)|}\right) \\ & +\tfrac{1}{c}\theta_b N(k_s)\dot{k}_s + \tfrac{1}{c}\dot{k}_s\end{aligned} \tag{69}$$

Integrating both sides of the equation yields:

$$\begin{aligned}V(t) - V(0) \le \quad & \int_0^t \frac{1}{c}\theta_b N(k_s(\tau))\dot{k}_s(\tau)d\tau + \int_0^t \frac{1}{c}\dot{k}_s(\tau)d\tau \\ & -\int_0^t\left[\frac{2H\rho(t)}{\overline{\delta}\rho(t) - s(t)}\left[\lambda_s s(t)^2 + \eta_s s(t)^{(p+q)/p}\right] - \widetilde{\lambda}_a\left(|\varepsilon(t)| + \eta_a e^{-|\varepsilon(t)|}\right)\right]d\tau\end{aligned} \tag{70}$$

$\frac{2H\rho(t)}{\overline{\delta}\rho(t)-s(t)}\left[-\lambda_s s(t)^2 - \eta_s s(t)^{(p+q)/p}\right] + \widetilde{\lambda}_a\left(|\varepsilon(t)| + \eta_a e^{-|\varepsilon(t)|}\right)$ is defined as S for later discussion.

Lemma 3 states that, $V(t) - V(0) + \int_0^t S d\tau$ is restricted, then S and $\int_0^t S d\tau$ are limited. According to Lemma 4, when $t \to \infty$, $s(t) \to 0$, thus $e(t) \to 0$, $\dot{e}(t) \to 0$.

The proof of Theorem 2 is complete. □

4. Numerical Simulation Results and Analysis

The effectiveness and robustness of the adaptive GFTSM controller based on the FTESO and PPC is proven through simulation in this section. Three different situations are offered for analysis:

Case 1: The ideal condition, where the FWUAV system has no parameter perturbation;
Case 2: The FWUAV experiences aerodynamic parameter perturbations, which lead to a 20% increase in lift and drag coefficient uncertainty and a 20% decrease in lateral force coefficient uncertainty;
Case 3: The FWUAV is susceptible to perturbations caused by wind in certain circumstances, resulting in nonlinear variations for the lift, drag, and lateral force coefficients, and the range of variations is 20%.

Case 1 is considered the fundamental reference. The initial attitude angle of the FWUAV is $\boldsymbol{\Theta}^{0b} = (\phi^{0b}, \theta^{0b}, \psi^{0b}) = (0, 0, 0)$ and the target attitude angle is $\boldsymbol{\Theta}^{0b} = (\phi^{0b}, \theta^{0b}, \psi^{0b}) = (36^\circ/\pi, 36^\circ/\pi, 0)$. The mass-actuated FWUAV system is simulated using PID and LADRC and then compared with the control method described in this paper. The table below illustrates the major parameters of the mass-actuated fixed-wing UAV.

The fundamental characteristics of the research subject in this paper are presented in Table 1.

Table 1. Basic parameters of the FWUAV.

Parameter	Value
Total mass	12 kg
Reference wing area value	0.6 m^2
Mass block in wing	1 kg
Mass block in fuselage	1 kg
Moment of inertia (without moving mass)	$J_{xx} = 0.8244$ kg·m^2 $J_{yy} = 1.135$ kg·m^2 $J_{zz} = 1.759$ kg·m^2 $J_{xz} = 0.1204$ kg·m^2
Span	4 m
Mean aerodynamic chord	0.1 m

As illustrated in Figure 6, the adoption of the controller proposed in this paper ensures that the response of the system's sliding mode surface is strictly confined within the specified range and enables the system state to quickly converge to the neighborhood of the sliding mode surface. The red dotted line represents the response of the controller's sliding mode surface function, while the black solid line indicates the upper and lower limits of the sliding mode surface function.

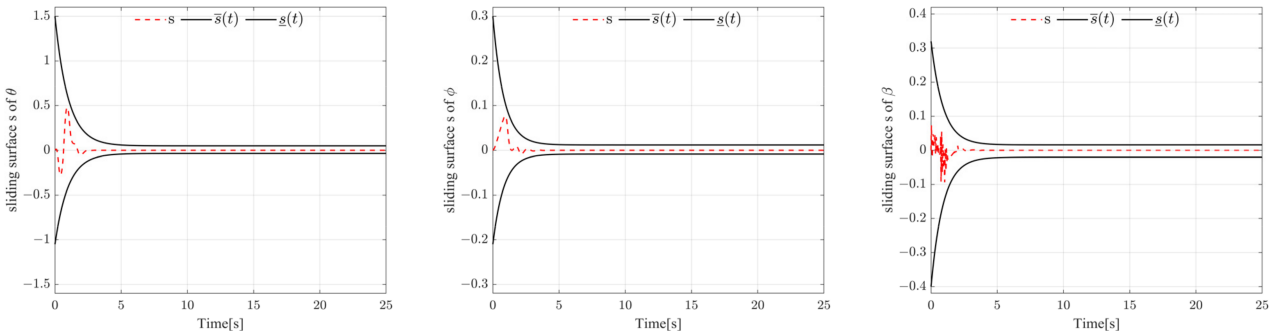

(**a**) (**b**) (**c**)

Figure 6. Response curves of sliding mode surface s. (**a**) The sliding mode surface responses for the pitch angle; (**b**) The sliding mode surface responses for the roll angle; (**c**) The sliding mode surface responses for the sideslip angle.

The flight results of each control method are displayed below. The red solid line shows the simulation results of the new adaptive GFTSM control approach described in this paper. The algorithm parameters are shown inTable 2. The green solid line represents the LADRC control method and the blue solid line represents the PID control method.

Table 2. Main controller parameters proposed in this paper.

Parameter	Roll Channel	Pitch Channel	Yaw Channel
θ_b	8.64	8.64	8.64
α_0	18	16	10
β_0	5	5	5
p_0	9	99	99
q_0	7	97	97
p	5	9	9
q	3	7	7
η_s	0	5	50
L	0	0.9	0.1
ϖ	80	250	80
τ_a	0.001	0.001	0.001
ε_a	0.0005	0.0005	0.0001
η_a	0.6	0.5	0.2

The change in attitude angle over time in Case 1 is depicted in Figure 7. It can be seen that the controller presented in this paper can converge to the target value within 2.5 s in the pitch channel, while the traditional LADRC and PID reach stability within 3.2 s and 12 s, respectively, and it is obvious that the controller presented in this paper has less overshoot than the other three control methods. And, the control method developed in this paper ensures rapid convergence speed and low overshoot in the roll channel. Moreover, both LADRC and the novel controller experience a certain chatter when the sideslip angle converges to 0 in a short period during the convergence process, but the maximum range of buffeting is in the order of 10^{-3}, so the effect is equivalent. It can be inferred that the controller proposed in this study has a faster response, smaller tracking error, and can perform fast and steady tracking of reference signals.

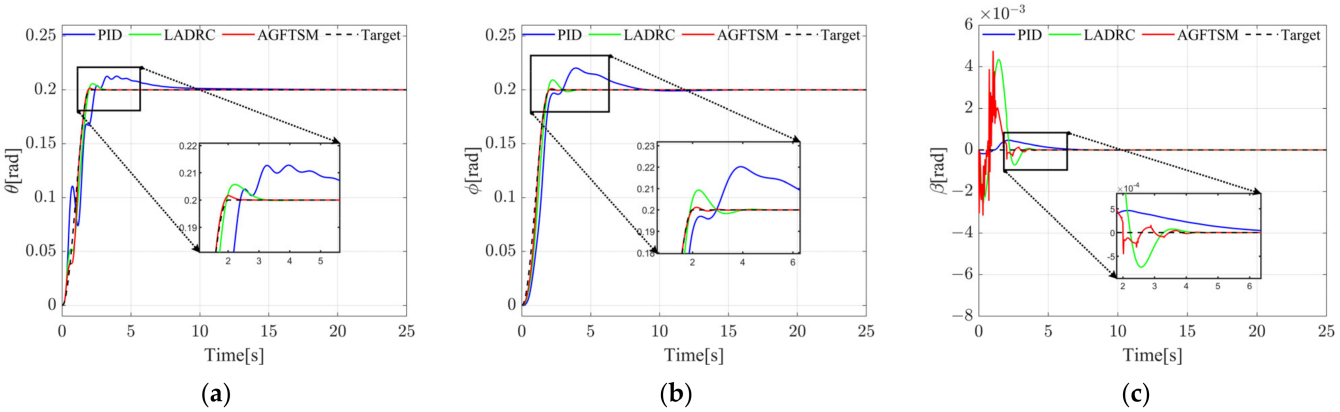

Figure 7. Attitude angle response curves in Case 1. (**a**) Pitch angle variations for the three methods; (**b**) Roll angle variations for the three methods; (**c**) Sideslip angle variations for the three methods.

Figure 8 shows the tracking error of the desired trajectory. The accuracy of the three control methods can be compared, and it is evident that the developed control method has superior accuracy. The response curves of attitude angular velocities are illustrated in Figure 9. The attitude control signals are depicted in Figure 10. Figure 11 displays the adaptive parameter simulations for pitch angle, roll angle, and sideslip angle in Case 1.

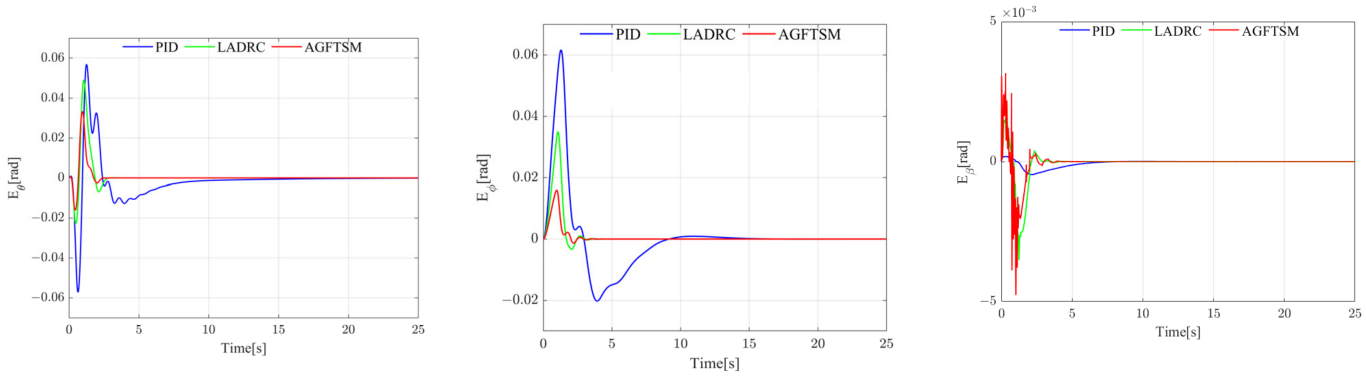

(**a**) (**b**) (**c**)

Figure 8. Tracking errors of the (**a**) pitch angle, (**b**) roll angle and (**c**) sideslip angle in Case 1.

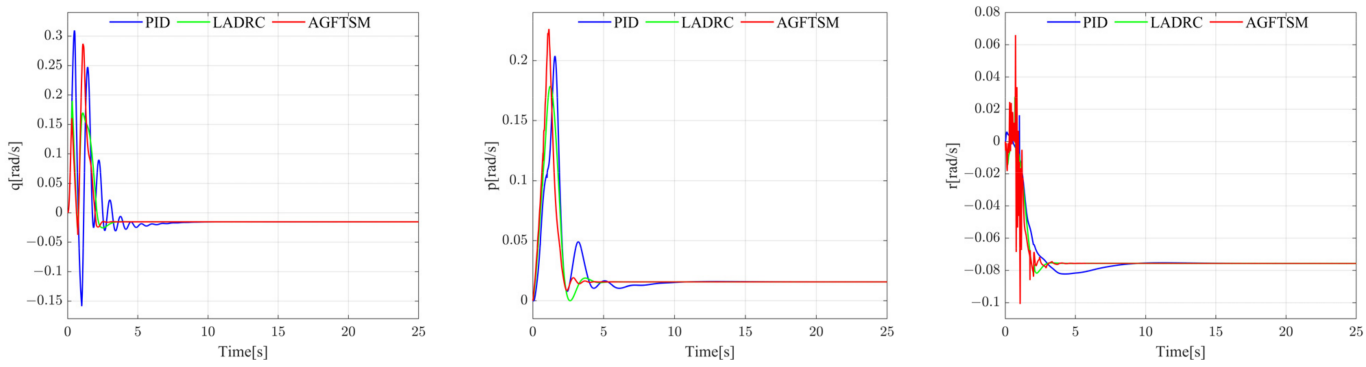

(**a**) (**b**) (**c**)

Figure 9. Response curves of (**a**) pitch angular velocity, (**b**) roll angular velocity, and (**c**) sideslip angular velocity in Case 1.

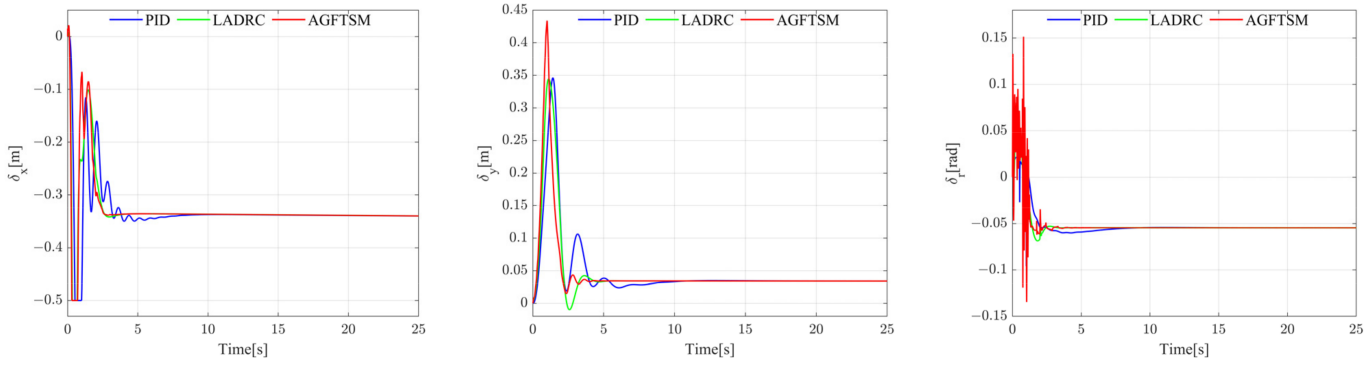

(**a**) (**b**) (**c**)

Figure 10. Attitude control signals for (**a**) pitch channel, (**b**) roll channel, and (**c**) yaw channel in Case 1.

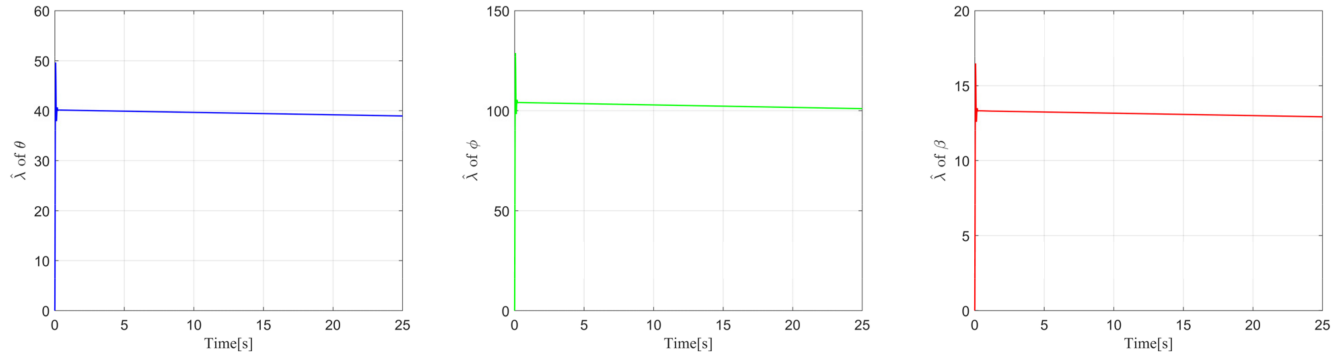

Figure 11. Simulations of adaptive parameters for (**a**) pitch angle, (**b**) roll angle, and (**c**) sideslip angle in Case 1.

The variations in attitude angles, tracking errors, attitude angular velocities, and control inputs under Case 2 are illustrated in Figures 12–15, accordingly. As revealed in Figure 12, the overshoot of pitch angle utilizing the proposed controller is comparable to that of LADRC, but with a significantly faster convergence rate. This advantage is also visible in the comparison of roll angle and side slip angle. Figure 16 presents the adaptive parameters for pitch angle, roll angle, and sideslip angle in Case 2.

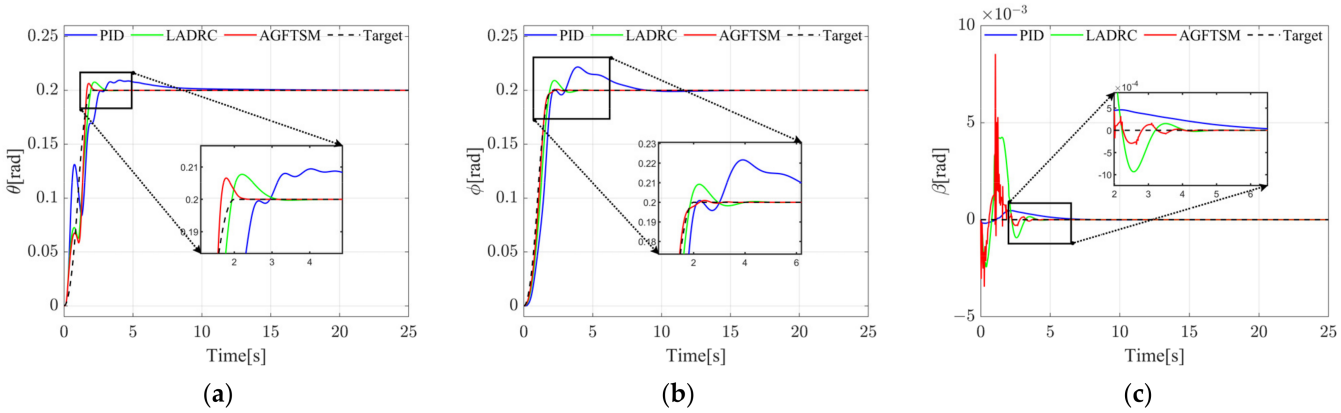

Figure 12. Attitude angle response curves in Case 2. (**a**) Pitch angle variations for the three methods; (**b**) Roll angle variations for the three methods; (**c**) Sideslip angle variations for the three methods.

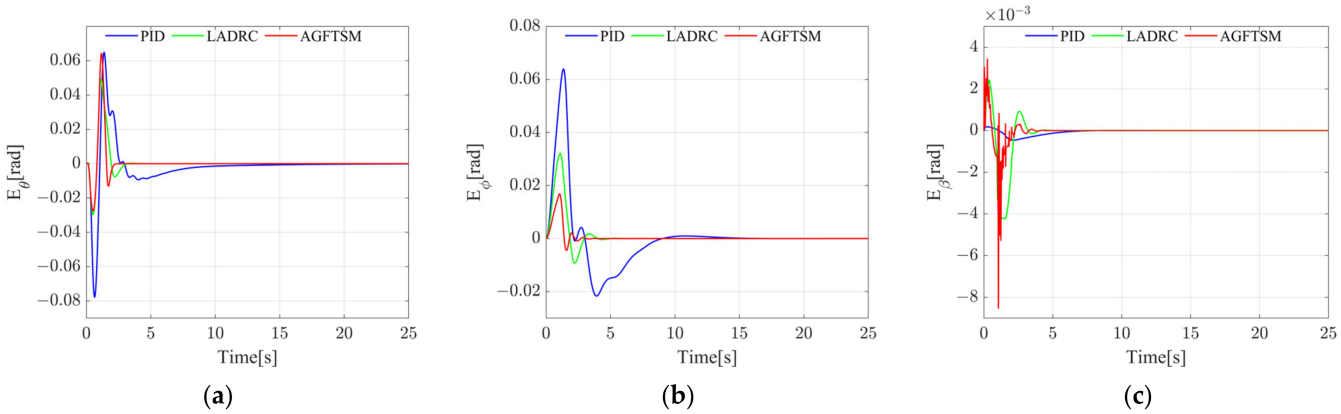

Figure 13. Tracking errors of (**a**) pitch angle, (**b**) roll angle and (**c**) sideslip angle in Case 2.

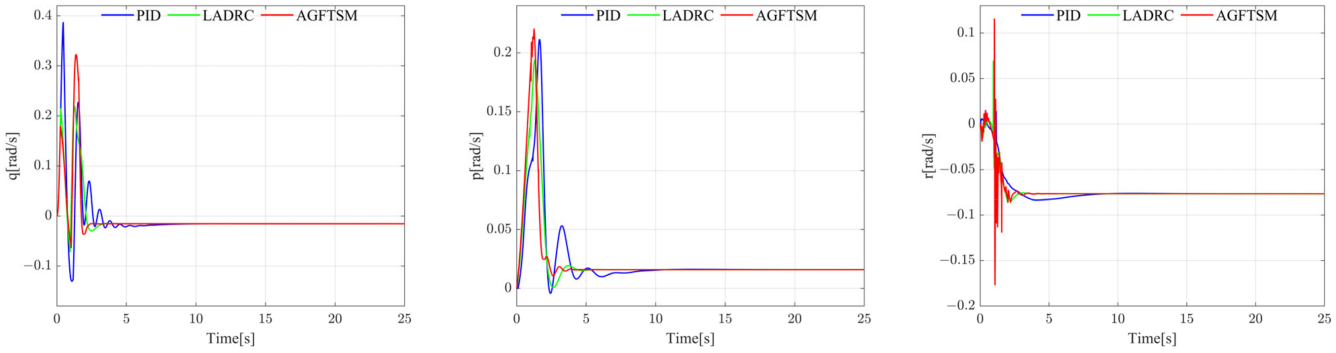

(**a**) (**b**) (**c**)

Figure 14. Response curves of (**a**) pitch angular velocity, (**b**) roll angular velocity, and (**c**) sideslip angular velocity in Case 2.

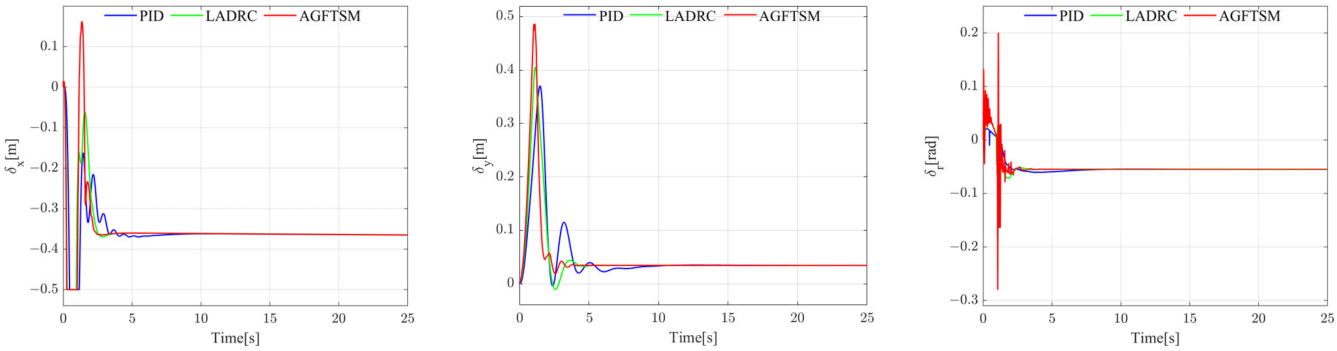

(**a**) (**b**) (**c**)

Figure 15. Attitude control signals for (**a**) pitch channel, (**b**) roll channel, and (**c**) yaw channel in Case 2.

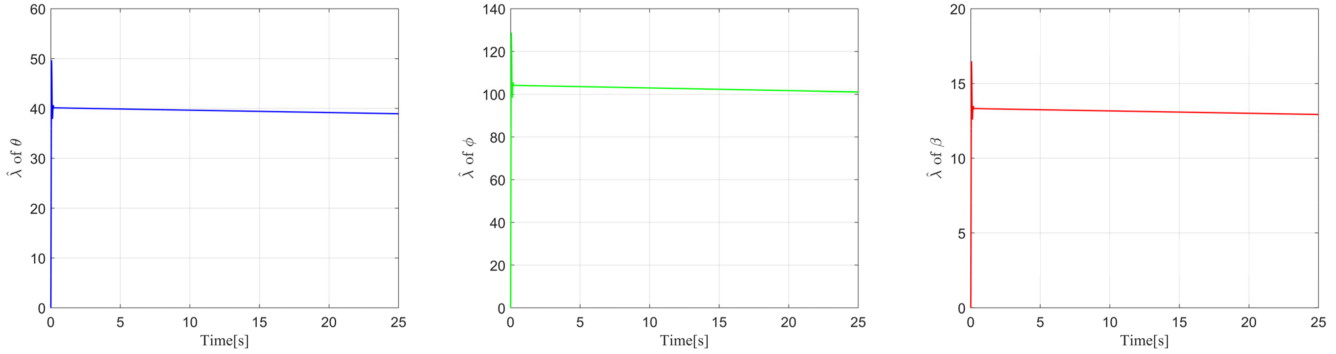

(**a**) (**b**) (**c**)

Figure 16. Simulations of adaptive parameters for (**a**) pitch angle, (**b**) roll angle, and (**c**) sideslip angle in Case 2.

In Figure 17, the changes in attitude angles are indicated under Case 3. The tracking errors are illustrated in Figure 18, while the attitude angular velocities are shown in Figure 19. Additionally, the control input variations are presented Figure 20 for the same working conditions. Due to the influence of nonlinear disturbance, the attitude angle tracking performance of PID and LADRC deteriorates, leading to increased amplitude of curve fluctuations. However, with the support of FTESO and adaptive law, the suggested controller is still able to perform speedy and precise target signal tracking. This clearly demonstrates the excellent stability and robustness of the controller designed in this paper.

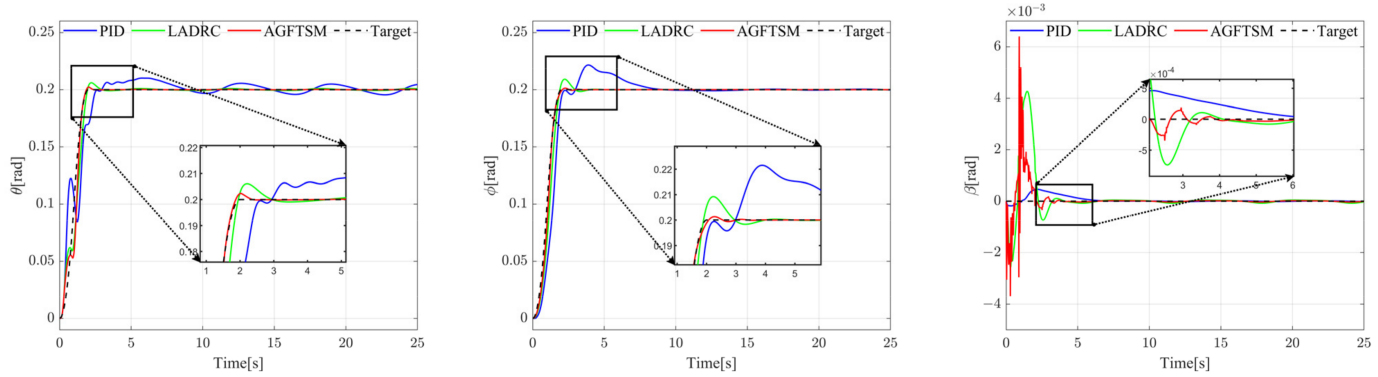

Figure 17. Attitude angle response curves in Case 3. (**a**) Pitch angle variations for the three methods; (**b**) Roll angle variations for the three methods; (**c**) Sideslip angle variations for the three methods.

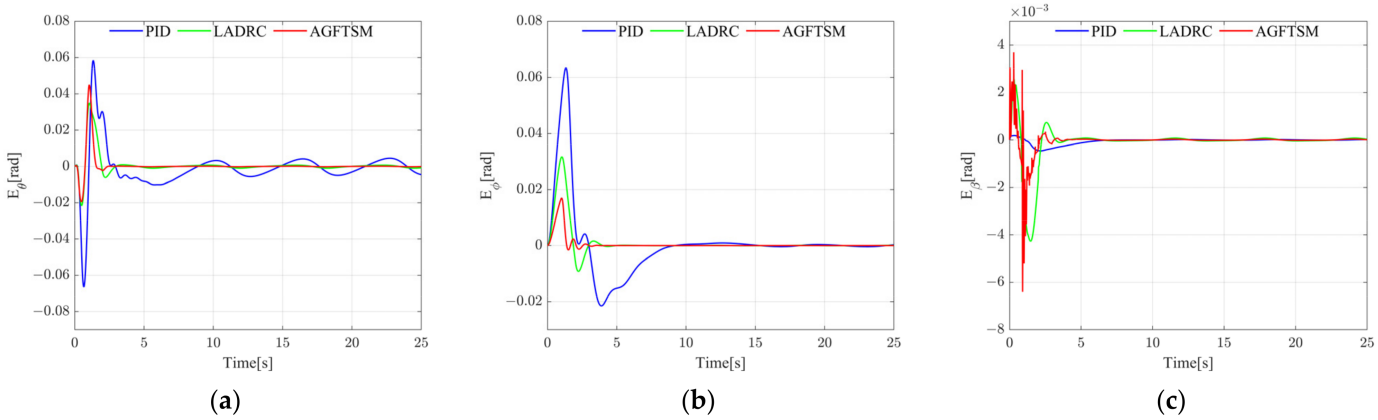

Figure 18. Tracking errors of (**a**) pitch angle, (**b**) roll angle and (**c**) sideslip angle in Case 3.

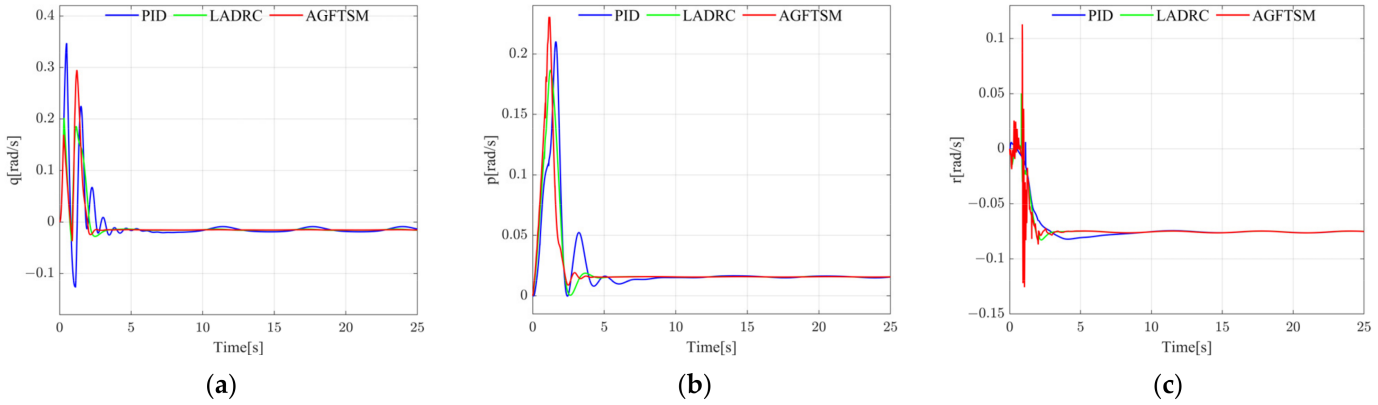

Figure 19. Response curves of (**a**) pitch angular velocity, (**b**) roll angular velocity, and (**c**) sideslip angular velocity in Case 3.

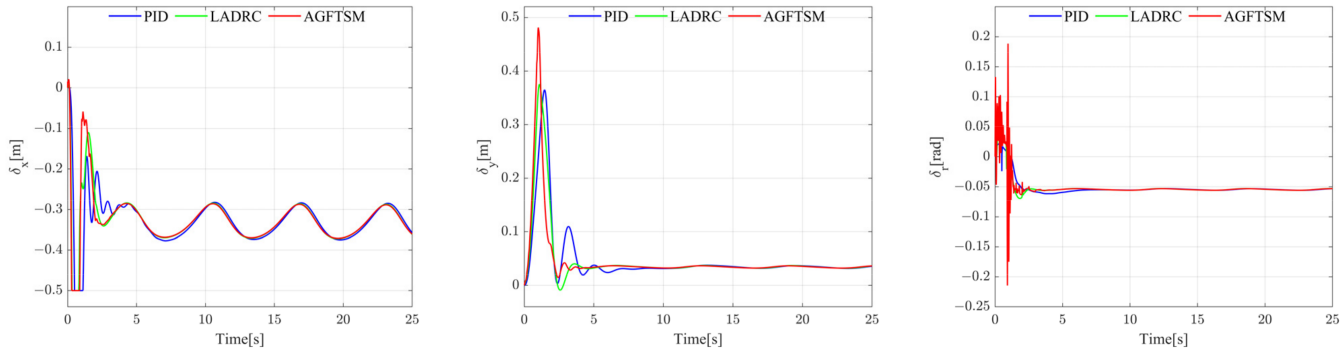

Figure 20. Attitude control signals for (**a**) pitch channel, (**b**) roll channel, and (**c**) yaw channel in Case 3.

Simulation curves of the adaptive parameters for the proposed FWUAV in each channel in Case 3 are depicted in Figure 21. It is evident from Figure 11, Figure 16, and Figure 21 that the curves converge rapidly and maintain stability.

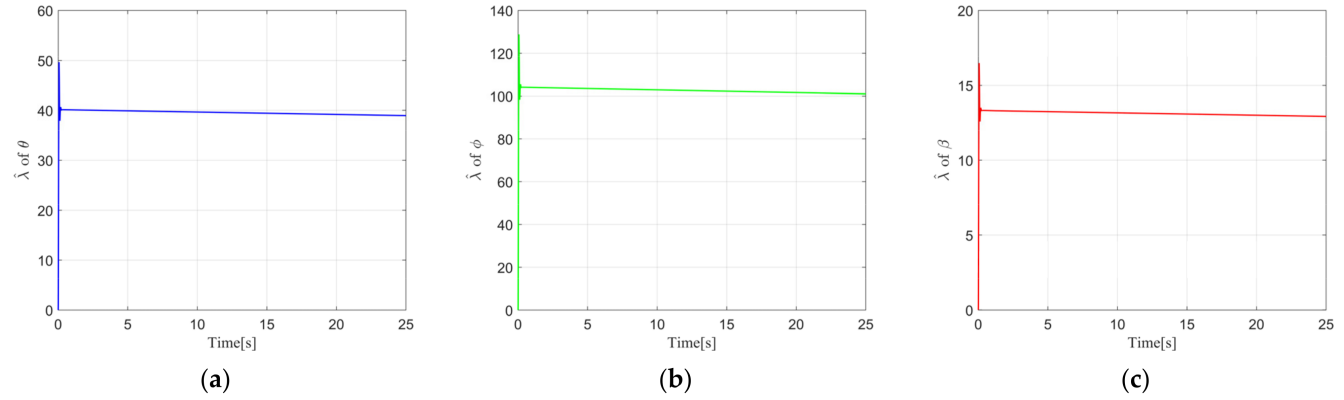

Figure 21. Simulations of adaptive parameters for (**a**) pitch angle, (**b**) roll angle, and (**c**) sideslip angle in Case 3.

The proposed controller's effectiveness and robustness were verified based on the provided flight trajectory. Figure 22 shows the target flight path.

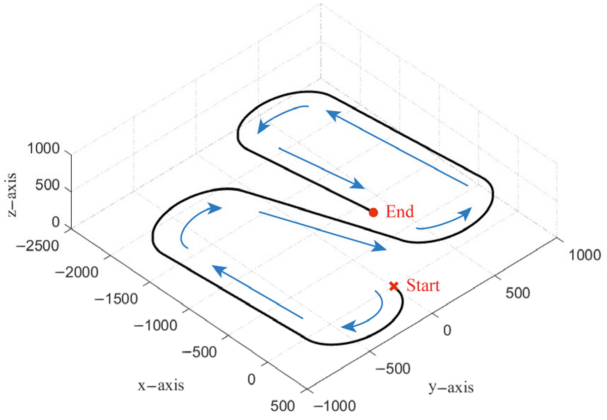

Figure 22. Target flight path.

The tracking results of the proposed controller for the attitude angle obtained from the flight trajectory are shown in Figures 23–25. It is evident that adaptive GFTSM controller

based on FTESO and PPC can reliably track the target signal under the required conditions, with good steady-state accuracy and dynamic characteristics, regardless of linear and nonlinear parameter perturbations. This demonstrates the excellent robustness and effectiveness of the controller.

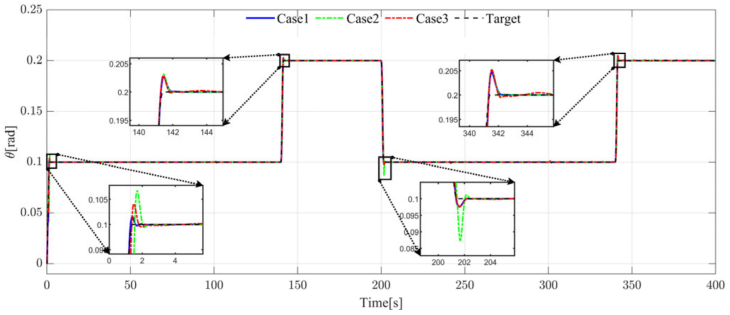

Figure 23. Response curves for tracking a desired trajectory under Case 1, 2, and 3.

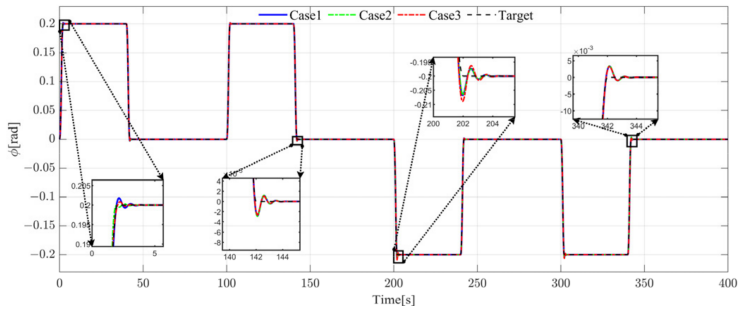

Figure 24. Response curves for tracking a desired trajectory under Case 1, 2, and 3.

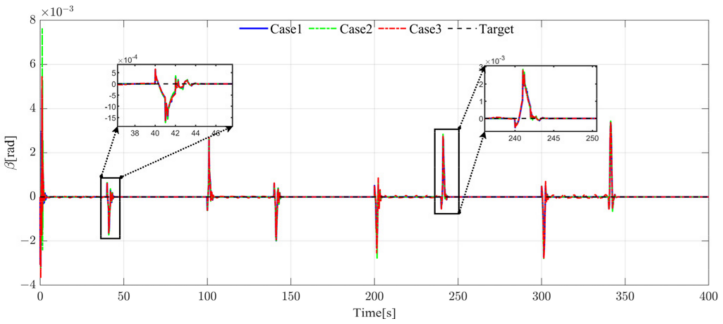

Figure 25. Response curves for tracking a desired trajectory under Case 1, 2, and 3.

5. Conclusions

This paper introduces a novel controller utilizing an adaptive GFTSM controller for a complicated system consisting of a dual-channel mass-actuated FWUAV. The proposed controller enhances the system's robustness and anti-interference capabilities. Employing the PPC theory guarantees both the transient and steady-state responses of the system. To lessen the effect of mass movement on inertial coupling, a FTESO is utilized to quickly and accurately track and eliminate the unknown term that this phenomenon creates. The stability of the closed-loop system is confirmed using Lyapunov stability analysis. The Simulink simulation results yielded the following conclusions:

1. The control method presented in this paper displays strong robustness and the ability to quickly and stably track the target signal;
2. The controller in this paper is compared with PID and LADRC controllers, and the results demonstrate that the controller designed in this paper is superior to the latter two in signal tracking;

3. To validate the effectiveness and robustness of the proposed controller in this paper for the target flight path, three operating conditions are described. The results reveal that the controller displays high steady-state accuracy and dynamic responsiveness under all three working circumstances, indicating its effectiveness and robustness.

Author Contributions: Conceptualization, J.Z. and L.Y.; methodology, J.Z.; software, J.Z.; validation, L.Y.; formal analysis, J.Z.; investigation, X.W.; resources, L.M.; data curation, L.M.; writing—original draft preparation, J.Z.; writing—review and editing, L.Y.; visualization, L.Y.; supervision, L.Y.; project administration, X.W.; funding acquisition, L.M. All authors have read and agreed to the published version of the manuscript.

Funding: This research received no external funding.

Data Availability Statement: Data are contained within the article.

Acknowledgments: The authors are grateful to the reviewers for their valuable suggestions.

Conflicts of Interest: The authors declare no conflicts of interest.

Appendix A

The detailed expressions of the matrixes in Equation (21) are presented as follows. In Equation (21), $x_3 = x_{3i}$, $b = b_{ii}$, and $u = u_i$, $(i = 1, 2, 3, 4, 5, 6)$.

$$\boldsymbol{x}_3 = \begin{bmatrix} x_{31} \\ x_{32} \\ x_{33} \\ x_{34} \\ x_{35} \\ x_{36} \end{bmatrix}$$

$$= -\begin{bmatrix} \boldsymbol{M}_b & -\boldsymbol{S}_b \\ \boldsymbol{S}_b & \boldsymbol{J}_b \end{bmatrix}^{-1} \left(\begin{bmatrix} \boldsymbol{M}_b \widetilde{\boldsymbol{\omega}}^{b0} & -\left(\widetilde{\boldsymbol{\omega}}^{b0} \boldsymbol{S}_b + 2\dot{\boldsymbol{S}}_b \right) \\ \boldsymbol{S}_b \widetilde{\boldsymbol{\omega}}^{b0} & \widetilde{\boldsymbol{\omega}}^{b0} \left(\boldsymbol{J}_b - 2\Sigma \widetilde{\boldsymbol{\rho}}_k^b \dot{\widetilde{\boldsymbol{\rho}}}_k^b \right) \end{bmatrix} \dot{\boldsymbol{y}} + \begin{bmatrix} \Sigma m_k \ddot{\boldsymbol{\rho}}_k^b \\ \Sigma m_k \widetilde{\boldsymbol{\rho}}_k^b \ddot{\boldsymbol{\rho}}_k^b \end{bmatrix} - \left(\begin{bmatrix} \boldsymbol{F}_{aero} \\ \boldsymbol{M}_{aero} \end{bmatrix} + \begin{bmatrix} \boldsymbol{F}_T \\ \boldsymbol{M}_T \end{bmatrix} \right) \right)$$

$$\boldsymbol{b} = \begin{bmatrix} b_{11} \\ b_{22} \\ b_{33} \\ b_{44} \\ b_{55} \\ b_{66} \end{bmatrix} = \begin{bmatrix} \boldsymbol{M}_b & -\boldsymbol{S}_b \\ \boldsymbol{S}_b & \boldsymbol{J}_b \end{bmatrix}^{-1} \begin{bmatrix} \boldsymbol{F}_G \\ -\widetilde{\boldsymbol{I}} \end{bmatrix}^T, \left(\boldsymbol{I} = \boldsymbol{A}^{b0} \boldsymbol{G} \right)$$

$$\boldsymbol{u} = \begin{bmatrix} u_1 \\ u_2 \\ u_3 \\ u_4 \\ u_5 \\ u_6 \end{bmatrix} = \begin{bmatrix} \boldsymbol{0} \\ \sum_{k=1}^{N_b} m_k \boldsymbol{\rho}_k^b \end{bmatrix}$$

References

1. Hakim, M.L.; Pratiwi, H.; Nugraha, A.C. Development of unmanned aerial vehicle (UAV) fixed-wing for monitoring, mapping and dropping applications on agricultural land. *J. Phys. Conf. Series. IOP Publ.* **2021**, *2111*, 012051. [CrossRef]
2. Liu, Z.; Wang, X.; Shen, L. Mission-oriented miniature fixed-wing UAV swarms: A multilayered and distributed architecture. *IEEE Trans. Syst. Man Cybern. Syst.* **2020**, *52*, 1588–1602. [CrossRef]
3. Sun, J.; Jing, W.; Gao, C. Attitude dynamics and control of high-mass-ratio fixed-trim moving mass reentry vehicle. *Aerosp. Sci. Technol.* **2022**, *123*, 107456. [CrossRef]
4. Robinett, R.D., III; Sturgis, B.R.; Kerr, S.A. Moving mass trim control for aerospace vehicles. *J. Guid. Control Dyn.* **1996**, *19*, 1064–1070. [CrossRef]

5. Li, B.; Su, T.C. Heading autopilot of autonomous underwater vehicles with internal moving mass. *J. Comput. Nonlinear Dyn.* **2017**, *12*, 021003. [CrossRef]
6. Huang, H.; Zhou, J. Solar sailing CubeSat attitude control method with satellite as moving mass. *Acta Astronaut.* **2019**, *159*, 331–341. [CrossRef]
7. Chen, L.; Zhou, G.; Yan, X.J. Composite control of stratospheric airships with moving masses. *J. Aircr.* **2012**, *49*, 794–801. [CrossRef]
8. Zhou, W.; Yin, K.; Wang, R. Design of attitude control system for UAV based on feedback linearization and adaptive control. *Math. Probl. Eng.* **2014**, *2014*, 492680. [CrossRef]
9. Zhang, J.; Li, Q.; Cheng, N. Non-linear flight control for unmanned aerial vehicles using adaptive backstepping based on invariant manifolds. *Proc. Inst. Mech. Eng. Part G J. Aerosp. Eng.* **2013**, *227*, 33–44. [CrossRef]
10. Castañeda, H.; Salas-Peña, O.S.; León-Morales, J. Robust flight control for a fixed-wing unmanned aerial vehicle using adaptive super-twisting approach. *Proc. Inst. Mech. Eng. Part G J. Aerosp. Eng.* **2014**, *228*, 2310–2322. [CrossRef]
11. Manzoor, T.; Xia, Y.; Zhai, D.H. Trajectory tracking control of a VTOL unmanned aerial vehicle using offset-free tracking MPC. *Chin. J. Aeronaut.* **2020**, *33*, 2024–2042. [CrossRef]
12. Rogers, J.; Costello, M. Control authority of a projectile equipped with a controllable internal translating mass. *J. Guid. Control Dyn.* **2008**, *31*, 1323–1333. [CrossRef]
13. Wang, L.L.; Yu, J.Q.; Wang, Y.F. Single moving-mass asymmetrical reentry vehicle modeling and control. *Syst. Eng. Electron.* **2015**, *37*, 1116–1123.
14. Erturk, S.; Daskiran, O.; Dogan, A. Trim analysis of a moving-mass actuated airplane. *AIAA Atmos. Flight Mech. Conf.* **2012**, 4647.
15. Erturk, S.A.; Dogan, A. Dynamic simulation and control of mass-actuated airplane. *J. Guid. Control Dyn.* **2017**, *40*, 1939–1953. [CrossRef]
16. Menon, P.; Vaddi, S.; Ohlmeyer, E. Finite-horizon robust integrated guidance-control of a moving-mass actuated kinetic warhead. *AIAA Guid. Navig. Control Conf. Exhib.* **2006**, 6787.
17. Gao, C.; Jing, W.; Wei, P. Research on application of single moving mass in the reentry warhead maneuver. *Aerosp. Sci. Technol.* **2013**, *30*, 108–118. [CrossRef]
18. Jia-Wang, L.I.; Bao-Wei, S.; Cheng, S. Tracking control of autonomous underwater vehicles with internal moving mass. *Acta Autom. Sin.* **2008**, *34*, 1319–1323.
19. Cao, C.; Hovakimyan, N. L1 adaptive output-feedback controller for non-strictly-positive-real reference systems: Missile longitudinal autopilot design. *J. Guid. Control Dyn.* **2009**, *32*, 717–726. [CrossRef]
20. Gao, C.; Li, J.; Fan, Y. Immersion and invariance-based control of novel moving-mass flight vehicles. *Aerosp. Sci. Technol.* **2018**, *74*, 63–71. [CrossRef]
21. Chen, H.; Zhou, J.; Zhou, M. Nussbaum gain adaptive control scheme for moving mass reentry hypersonic vehicle with actuator saturation. *Aerosp. Sci. Technol.* **2019**, *91*, 357–371. [CrossRef]
22. Ahmed, S.; Azar, A.T. Adaptive fractional tracking control of robotic manipulator using fixed-time method. *Complex Intell. Syst.* **2024**, *10*, 369–382. [CrossRef]
23. Ahmed, S.; Azar, A.T.; Tounsi, M.; Ibraheem, I.K. Adaptive Control Design for Euler–Lagrange Systems Using Fixed-Time Fractional Integral Sliding Mode Scheme. *Fractal Fract.* **2023**, *7*, 712. [CrossRef]
24. Ahmed, S.; Azar, A.T.; Ibraheem, I.K. Nonlinear system controlled using novel adaptive fixed-time SMC. *AIMS Math.* **2024**, *9*, 7895–7916. [CrossRef]
25. Ahmed, S.; Azar, A.T.; Ibraheem, I.K. Model-free scheme using time delay estimation with fixed-time FSMC for the nonlinear robot dynamics. *AIMS Math.* **2024**, *9*, 9989–10009. [CrossRef]
26. Yue, T.; Zhang, X.; Wang, L. Flight dynamic modeling and control for a telescopic wing morphing aircraft via asymmetric wing morphing. *Aerosp. Sci. Technol.* **2017**, *70*, 328–338. [CrossRef]
27. Basin, M.; Yu, P.; Shtessel, Y. Finite-and fixed-time differentiators utilising HOSM techniques. *IET Control Theory Appl.* **2017**, *11*, 1144–1152. [CrossRef]
28. Wang, X.; Lin, H. Design and frequency analysis of continuous finite-time-convergent differentiator. *Aerosp. Sci. Technol.* **2012**, *18*, 69–78. [CrossRef]
29. Bhat, S.P.; Bernstein, D.S. Finite-time stability of continuous autonomous systems. *SIAM J. Control Optim.* **2000**, *38*, 751–766. [CrossRef]
30. Zhang, L.; Wei, C.; Wu, R.; Cui, N. Fixed-time extended state observer based non-singular fast terminal sliding mode control for a VTVL reusable launch vehicle. *Aerosp. Sci. Technol.* **2018**, *82*, 70–79. [CrossRef]
31. Tian, B.; Zuo, Z.; Yan, X. A fixed-time output feedback control scheme for double integrator systems. *Automatica* **2017**, *80*, 17–24. [CrossRef]
32. Nussbaum, R.D. Some remarks on a conjecture in parameter adaptive control. *Syst. Control Lett.* **1983**, *3*, 243–246. [CrossRef]
33. Xudong, Y.; Jingping, J. Adaptive nonlinear design without a priori knowledge of control directions. *IEEE Trans. Autom. Control* **1998**, *43*, 1617–1621. [CrossRef]

34. Ioannou, P.A.; Sun, J. *Robust Adaptive Control*; PTR Prentice-Hall: Upper Saddle River, NJ, USA, 1996.
35. Plestan, F.; Shtessel, Y.; Brégeault, V. Sliding mode control with gain adaptation—Application to an electropneumatic actuator. *Control Eng. Pract.* **2013**, *21*, 679–688. [CrossRef]